

**EVALUATING THE SEPARATION OF STEAM-ASSISTED GRAVITY
DRAINAGE EMULSIONS USING HIERARCHICALLY TEXTURED
MEMBRANES**

A Thesis

by

FRANK-ERIC NGAMASSI KAMTCHE

Submitted to the office of Graduate and Professional Studies of
Texas A&M University
In partial fulfillment of the requirements for the degree of

MASTER OF SCIENCE

Committee Chair,	Sarbajit Banerjee
Co-Chair of Committee,	Partha Mukherjee
Committee Members,	Stratos Pistikopoulos
Intercollegiate Faculty Chair,	Christodoulos A. Floudas

August 2017

Major Subject: Energy

Copyright 2017 Frank-Eric Ngamassi Kamtche

ABSTRACT

Removing submicrometer-sized oil droplets from water is still one of the leading challenges in the separation of emulsions. In the oil and gas industry, emulsions are handled in one of two distinctive ways: the stabilization of emulsions is altogether precluded by the addition of appropriate demulsifiers or emulsions are separated after extraction. During the extraction of hydrocarbons, it is possible to use preventive measures that greatly mitigate the formation of emulsions. However, the increased usage of unconventional extractive processes such as steam-assisted gravity drainage (SAG-D) where emulsions form easily as a result of natural surfactants, makes such preventive measures impractical and can furthermore reduce the efficacy of the extractive processes. Engineering the separation of emulsions has thus emerged as a critical imperative. The separation of emulsions has further resonance in addressing oil spills in marine environments. In this work, we demonstrate that a mesostructured substrate with hierarchical texturation shows drastic differences in the wettability of water and oil. The mesostructured substrates are prepared using a scalable process in which ZnO nanotetrapods, prepared by oxidizing zinc metal at high-temperature, are spray coated onto a stainless-steel mesh that exhibits microscale texturation. The ability of such meshes to separate the water and oil fractions of SAG-D emulsions and the flux rates attainable for such a separation process have been evaluated as a function of mesh pore size and ZnO loading. The use of high temperatures was necessary for the separation given the operating conditions under which the emulsions are extracted and handled. Such high temperatures are required to break apart complex emulsions. Based on the results obtained, membranes with small pore sizes are necessary to significantly reduce the quantity of water

present in the emulsions. The flux rate also showed a great variance between high and low permeation temperatures as well as high and low ZnO concentrations.

DEDICATION

I dedicate this thesis to my family.

ACKNOWLEDGEMENTS

I would like to express my greatest gratitude to my advisor, Dr. Sarbajit Banerjee, for his support and guidance throughout this research at Texas A&M University. I am extremely grateful to Thomas O'Loughlin and the entire Banerjee research group for everything they taught me at the Banerjee laboratory. I would like to thank Dr. Partha Mukherjee, and Dr. Stratos Pistikopoulos for being on my committee. Special thanks to Dr. Valentini Pappa, who kept me motivated throughout the research period. I am forever grateful for my parents, Dr. Louis-Marie and Madeleine-Irene Ngamassi. Without them I would not be where I am today. To my siblings, Laetitia, Hermann Ngamassi and Sandra Fomete, thank you for always cheering me on. I would like to thank Alexander Tankou, and Kojo Acheampong for being great friends. To my roommates, Roby Nkwamo and Christian Kana Nguene, thanks for the memories we shared at Texas A&M University.

CONTRIBUTORS AND FUNDING SOURCES

Contributors

This work was supervised by a thesis dissertation committee consisting of Professor Sarbajit Banerjee and Professor Partha Mukherjee of the Department of Mechanical Engineering and Professor Stratos Pistikopoulos of the Department of Chemical Engineering.

All work for the thesis dissertation was completed by the student, in collaboration with Thomas O'Loughlin of the Department of Chemistry.

Funding Sources

The research was funded in part by Cenovus Energy Inc.

TABLE OF CONTENTS

	Page
ABSTRACT.....	ii
DEDICATION.....	iv
ACKNOWLEDGEMENTS.....	v
CONTRIBUTORS AND FUNDING SOURCES.....	vi
TABLE OF CONTENTS.....	vii
LIST OF FIGURES.....	viii
LIST OF TABLES.....	x
CHAPTER I INTRODUCTION AND MOTIVATION.....	1
1.1 Steam Assisted Gravity Drainage.....	1
1.2 Wettability.....	4
CHAPTER II AUTOCLAVE REACTOR COMMISSIONING.....	7
2.1 Commissioning of a High-Pressure and High-Temperature Vessel.....	7
2.2 Inserts for Filtration.....	18
CHAPTER III CHARACTERIZATION OF MEMBRANE STRUCTURE AND FUNCTION.....	21
3.1 Growth of ZnO Tetrapods.....	21
3.2 Preparation of membrane by spray coating of ZnO onto stainless steel mesh.....	25
3.3 Characterization of SAG-D emulsions.....	28
3.4 Evaluation of the efficacy of the hierarchically textured membranes.....	30
3.5 Membrane Performance.....	33
CHAPTER IV CONCLUSIONS AND FUTURE DIRECTIONS.....	43
REFERENCES.....	45

LIST OF FIGURES

	Page
Figure 1: Schematic of a steam assisted gravity drainage method	3
Figure 2: Optical microscopy image of a reconstituted bitumen emulsion that is untreated (not permeated)	9
Figure 3: Engineering drawing of the reactor with all the parts labeled	11
Figure 4: Schematic depiction of the autoclave reactor	12
Figure 5: Plots for commissioning of the autoclave reactor with deionized water at different temperatures and pressures	14
Figure 6: Plots for commissioning of the autoclave reactor with deionized water at different temperatures and pressures.	15
Figure 7: Plots for commissioning of the autoclave reactor with deionized water at different temperatures and pressures	16
Figure 8: Plots for commissioning of the autoclave reactor with deionized water at different temperatures and pressures	17
Figure 9: Plots for commissioning of the autoclave reactor with deionized water at different temperatures and pressures	18
Figure 10: Digital photographs of the filtration parts and how they are assembled for deployment under high-pressure and high-temperature conditions	19
Figure 11: Digital photographs acquired before and after separation of the emulsion	20
Figure 12: (A) Digital photograph of zinc metal substrates and (B) Powders of ZnO collected after the substrates were heated for 1 min at 950°C	22
Figure 13: Schematic representation of the apparatus used for generation of ZnO tetrapods	23

Figure 14: Thermal ramping profile used to grow ZnO nanotetrapods	23
Figure 15: Representative X-ray diffraction pattern	24
Figure 16: SEM images depicting the multiscale textured metal meshes modified by the deposition of ZnO nanotetrapods at various magnifications	26
Figure 17: Digital photograph of meshes used for the investigation	28
Figure 18: Optical microscopy image of a reconstituted bitumen emulsion that is untreated (not permeated)	29
Figure 19: Schematic representation of the separation process	31
Figure 20: Digital photograph of the Dean-Stark placed above a round-bottom flask	32
Figure 21: 3D Plot depicting the variation of the permeation temperature behavior as a function of the pore size and ZnO loading on the membrane	34
Figure 22: 3D Plot depicting the variation of the water content percentage as a function of the pore size and ZnO loading on the membrane	36
Figure 23: Optical microscopy of a reconstituted bitumen emulsion that permeated through a 250-gauge mesh with a pore size of 61 μm	19
Figure 24: Optical microscopy of a reconstituted bitumen emulsion that permeated through a 325-gauge mesh with a pore size of 43 μm	38
Figure 25: Optical microscopy of a reconstituted bitumen emulsion that permeated through a 400-gauge mesh with a pore size of 38 μm	39
Figure 26: Optical microscopy of a reconstituted bitumen emulsion that permeated through a 500-gauge mesh with a pore size of 30 μm	40
Figure 27: Plots showing the flux rate behavior with respect to the pore size, pore area and also, ZnO loadings on the membrane	42

LIST OF TABLES

	Page
Table 1: Rating Scale for tape test in ASTM D3359	27

CHAPTER I

INTRODUCTION AND MOTIVATION

1.1 Steam Assisted Gravity Drainage

Although there has been an increase in the usage of renewable energy, the continued dependence of global economies on fossil fuels cannot be understated. In order to meet global demand for fossil fuels, accessing unconventional geological deposits such as the Canadian Oil Sands in Northern Alberta and Saskatchewan has emerged as a critical imperative. According to the Energy Information Administration (EIA), current estimates suggest that the Canadian Oil Sands hold ca. 170 billion barrels of readily accessible deposits, which could meet the energy needs of the world for ca. 100 years given Canada's current production rate of ca. 4.6 million barrels per day [1].

Producing heavy oil is a very demanding task mainly due to its remarkably high viscosity under reservoir conditions. A wide spectrum of methods is used to extract heavy oil from the reservoir. Some of them are chemical approaches (polymers, surfactants), a class of methods denoted as miscible extraction (involving CO₂ injection, inert gases, or miscible solvents) and the steam assisted gravity drainage (SAG-D) method [2]. Given that the bitumen viscosity is sensitive to temperature, the SAG-D method has recently gained popularity for heavy oil extraction [3]. The idea of SAG-D was initially introduced in the 1970's by Dr. Roger Butler an engineer at Imperial Oil from 1955 to 1982 [4]. In this process, which is shown in figure 1, two parallel horizontal oil wells are drilled into the geological formation. The wells are placed vertically about 4 m to 10 m from each other. The steam is injected continuously from the injection well into a growing steam chamber. As the steam enters the

chamber, it moves to the edge of the chamber and condenses. As the temperature in the steam chamber increases the cold oil becomes less viscous and flows, reaching the production well [5].

In the presence of surfactants and upon extensive mechanical agitation induced by rapid steam injection and subsurface fluid flow, the suspended water droplets can be quite stable in terms of their dispersion. The resulting extracted liquids are emulsions of hydrocarbons and water. Depending on the relative content of the two liquids, oil-in-water or water-in-oil emulsions are stabilized. Hierarchical complex emulsions are often generated. Bringing about the efficacious separation of the water and oil components of the emulsions, particularly the separation of emulsified oil, is imperative both for increasing the efficiency of the extractive processes as well as to meet regulatory requirements for the treatment of wastewater (produced water) [6].

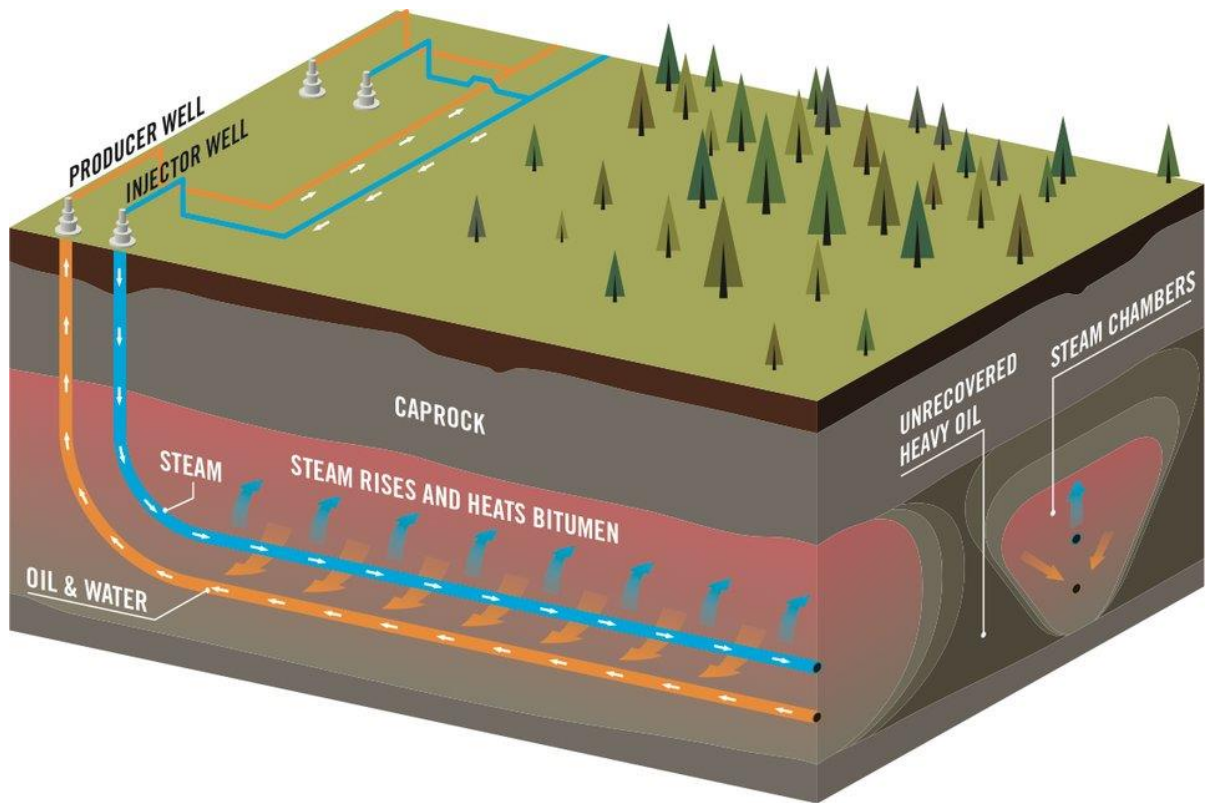


Figure 1: Schematic of a steam assisted gravity drainage method. Reproduced with permission from Connacher Oil & Gas/jwnenergy.com [7]

The major advantage that the SAG-D method has over other conventional steam flooding methods is that in SAG-D, the temperature in the steam chamber is constant and the same as that of the temperature of the steam. This means that the SAG-D bitumen stays hot as it flows to the production well. In contrast, in conventional steam flooding, the bitumen cools as it flows to the production well [8]. The primary focus of this dissertation will be to engineer the separation of realistic emulsions obtained from production wells based on orthogonal wettability of hydrocarbons and water towards nanotextured surfaces.

1.2 Wettability

When a liquid droplet comes into contact with a surface, the way it spreads on the surface and the shape of the droplet is determined by the balance between the interfacial energies.

When a liquid droplet contacts a surface, the solid-vapor interface is replaced by new liquid-vapor and vapor-liquid interfaces. The equilibrium contact angle (θ_e) captures the balance between the two interfacial energies and is represented as:

$$\cos\theta_e = \frac{\gamma_{SV}-\gamma_{SL}}{\gamma_{LV}} \dots\dots (1)$$

where θ_e is the equilibrium contact angle, γ_{sv} represents the interfacial energy of the solid/vapor surface, γ_{sl} represents the solid/liquid surface, and γ_{lv} represents the liquid/vapor surface [9]. Based on this simple formulation for the contact angle of a flat substrate, an initial idea for engineering orthogonal wettability can be developed. For a surface to be non-wettable to a liquid, the equilibrium contact angle θ_e should be at least 120° , therefore yielding a $\cos \theta_e$ value of -0.5. This implies that the interfacial energy at the solid-liquid interface (γ_{sl}) must be greater than the interfacial energy at the solid-vapor interface (γ_{sv}). Otherwise stated, the intrinsic surface energy of the solid-vapor energy must be very low, whereas that of the solid-liquid interface must be very high [10]. Conversely, the intrinsic surface energy that corresponds to the solid-vapor surface energy must be greater than the solid-liquid surface energy for the liquid to completely wet the surface [11]. Taking the wettability of a single surface by two different liquids into account, the γ_{sv} term is identical for both cases. This means that the sign and magnitude of $\cos\theta_e$ and the wettability of the two liquids depends ultimately on the numerical value of γ_{sl} with respect to γ_{sv} . This equilibrium is strongly affected by two parameters, which are as follows: (a) the surface

tension of the liquid, and (b) the chemical interaction of the surface and the liquid. This analysis therefore points out that two liquids with different values of solid-liquid interfacial energies (γ_{SL}), given a range of solid-vapor interfacial energies (γ_{SV}), can yield opposite signs of $\cos\theta_e$ for the same surface. This will therefore allow one liquid to be retained on the surface and the other to flow across without wetting the surface. In the case of a membrane configuration, the retained liquid will be able to permeate the membrane while the orthogonally wettable liquid continues to flow across the surface of the membrane.

Water and hydrocarbons have drastically different surface tension values, with very distinctive modes of intermolecular interactions at the surfaces. The surface tension of water is 72.80×10^{-3} N/m, whereas most hydrocarbons have a surface tension that is a third of this value. For example, decane and hexadecane have surface tension values of 23.83×10^{-3} N/m and 27.47×10^{-3} N/m at room temperature, respectively [12]. The smaller value of surface tension indicates that the solid-liquid interfacial energy (γ_{SL}) term is smaller, and thus these liquids are more likely to wet a surface. This therefore implies that using membranes with defined set of surface energies, it should be possible to separate water and oil by wetting hydrocarbons while remaining impervious to water.

The surface roughness of a substrate can greatly enhance the interfacial surface area or alter the proportion of the surface across which the solid and liquid are actually in contact. To account for surface roughness, equation 1 above is modified and the wettability observed for the rough surface can be written as:

$$\cos\theta_w = \frac{r(\gamma_{SV}-\gamma_{SL})}{\gamma_{LV}} = r\cos\theta_e \dots\dots (2) [13], [14]$$

Here, θ_w is the contact angle that is observed, r represents the ratio of the surface area to the surface area of an equivalent smooth surface, and θ_e is the equilibrium contact angle. In other words, while surface roughness cannot change the sign of the wettability, the magnitude of the observed $\cos\theta_w$ can be amplified. This means that for two liquids that have opposite signs of $\cos\theta$, surface roughness serves to exacerbate the differences in wettability [13], [15]–[17]. Simply put, for two liquids that present opposite signs of $\cos\theta$, surface roughness serves to exacerbate the differences in wettability, allowing for improved separation of the liquids. The focus of this work is to translate proof-of-concept separations previously observed using hexadecane/water emulsions to the separation of real SAG-D emulsions and to thereby design membranes that show separation based on differential wettability at high temperatures [9].

CHAPTER II

AUTOCLAVE REACTOR COMMISSIONING

2.1 Commissioning of a High-Pressure and High-Temperature Vessel

With the increasing emphasis on the tapping of unconventional deposits and an unfavorable regulatory environment, much recent attention has been focused on the development of membranes and demulsification methods for the separation of water/oil emulsions based on differential affinity, density, flow characteristics, and wettability [18]–[25]. De-emulsification is the industry standard but requires the use of large volumes of chemicals, long periods of time to allow complete settling, and is of limited efficacy in terms of removal of sub-micron-sized droplets. Membranes for separation make use of polymeric systems that have limited viability at the high temperatures and high pressures typical of industrial processes and further tend to be susceptible to degradation and sloughing. In this work, we explore the utility of an entirely inorganic system for separating the water and oil components of emulsions based on the differential wettability of the two liquids by utilizing a hierarchically textured metal mesh surface prepared by spray-coating nanostructured ZnO tetrapods onto microstructured stainless steel meshes [9]. Conventional filtration systems are unable to separate emulsions that consist of different droplet sizes of one phase within a second phase. Systems as such are generally built to separate oil and water droplets based on droplet size differentials. The issue however is that this filtration method requires that the pore size of the membrane be smaller than the smallest droplet size contained within the emulsion. This is seen as a challenge for submicron size droplets of emulsified oil because at high pressure, the droplets can be deformed and can break through the membrane, which

ends up substantially degrading the separation efficiency [20], [24]–[26]. Membranes with submicron-sized dimensions are often used to mitigate this problem but require unrealistically high pressure gradients and yield extremely low liquid fluxes [25]. Furthermore, as depicted in the optical micrograph of Figure 2, SAG-D emulsions have a complex hierarchical structure with oil droplets dispersed within a continuous water phase containing water droplets that further contain asphaltene residues. Separation exploiting simply a size differential at low temperatures would not be able to remove water droplets trapped within oil droplets. Given the stability of emulsions at room temperature, the use of higher temperatures is imperative to “crack” the emulsions. Consequently, membranes are required that provide selective permeability at high temperatures and that essentially ought to be impermeable at low temperatures.

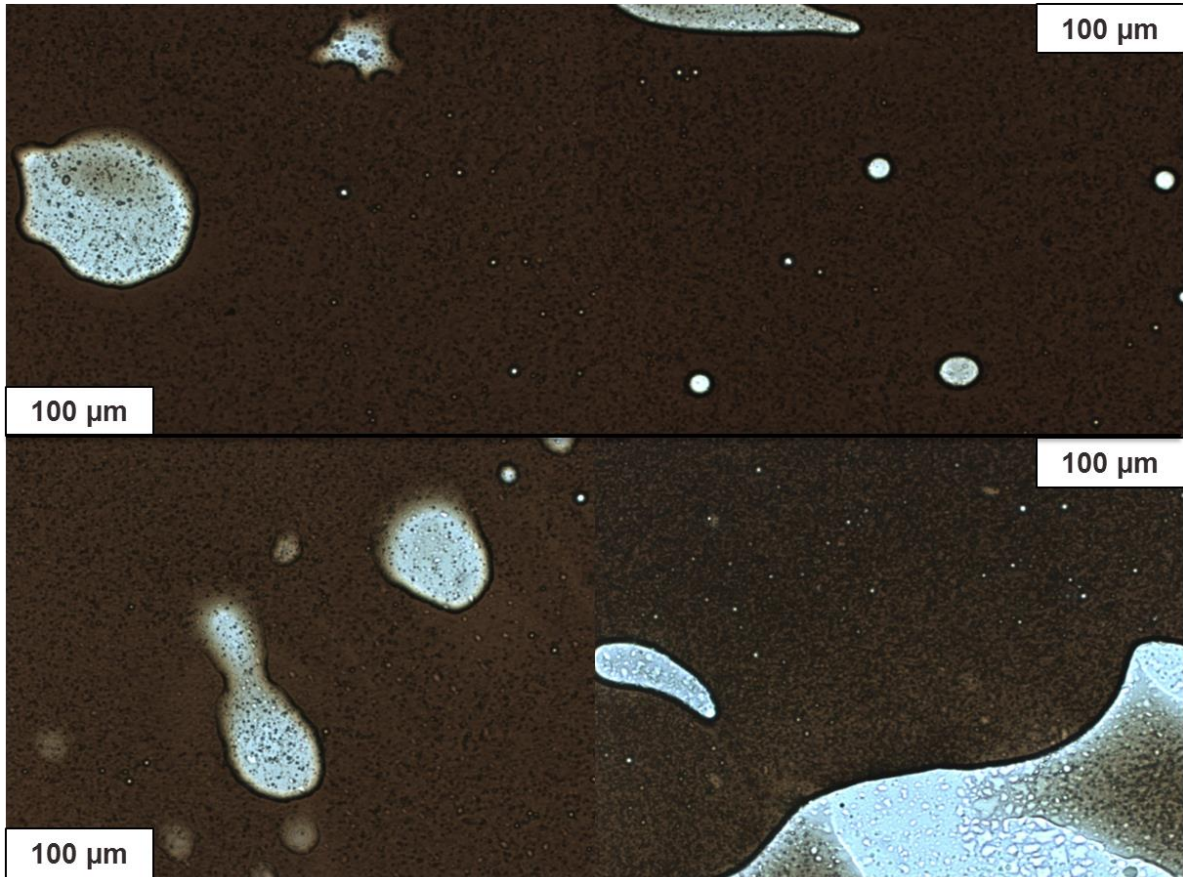


Figure 2: Optical microscopy image of a reconstituted bitumen emulsion that is untreated (not permeated). The lighter regions correspond to water droplets. Note that there are also some oil droplets embedded within the water droplets. The water content is estimated to be ca. 30 vol. % in this sample as per Dean-Stark's method. Darker solid particles are asphaltene residues.

In order to mimic realistic conditions, an autoclave reactor from Parr (Fig. 3) was chosen due to its ability to replicate high pressure and high temperatures. This reactor was selected due to its maximum operating temperature of 225°C and a pressure of 1034.21 kPa, while having a glass manifold that allows for real-time observation of fluid flow in the separation system. The autoclave sustains two types of temperature ramps. In the high heating option, the heater develops full power of 550 W. In the low heating option, the system only allows one half of the rated wattage to be supplied to the heater (Fig. 3). In general, the low heating option is most useful when the reactor is operating at temperatures below 175°C because rapid heating can lead to overheating.

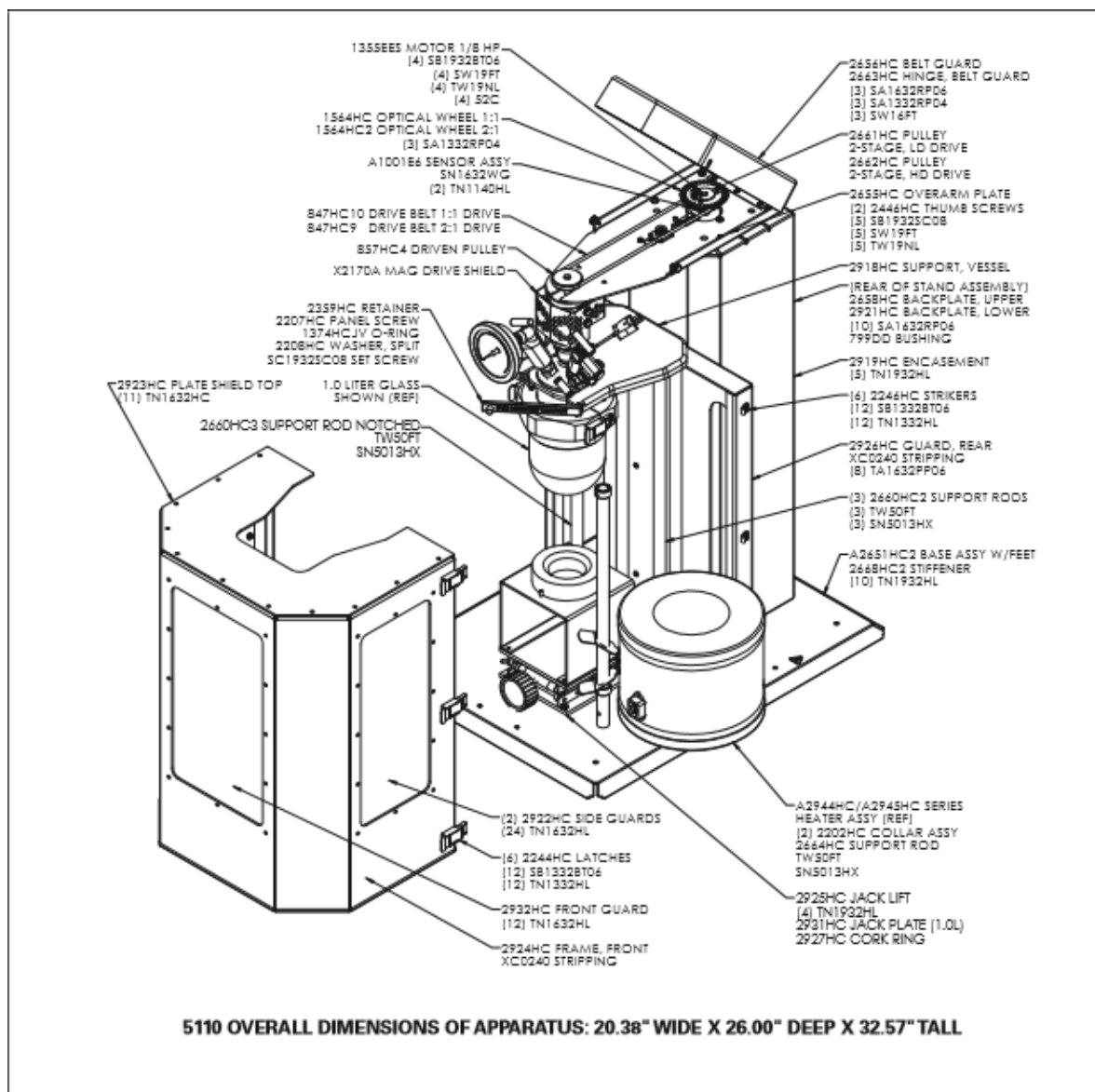


Figure 3: Engineering drawing of the reactor with all the parts labeled. Reproduced with permission from Parr Instrument Company, Moline, Illinois [27]

Figure 4 displays a schematic representation of the autoclave reactor vessel's setup and safety. To accommodate the custom fabricated autoclave reactor vessel inserts discussed later in this chapter, the largest volume of the autoclave reactor vessel (1.5L) was selected (Fig. 4A). A metal stand was used to stabilize this vessel while loading and unloading the samples.

Also, the heating mantle swivels to the side to allow for easy loading and unloading. The heating mantle can be further lowered to quickly and easily observe the vessel. For safety purposes, the autoclave reactor vessel's protective shield is placed, and later the fume hood sash is lowered to offer additional layer of protection from any venting of gasses.

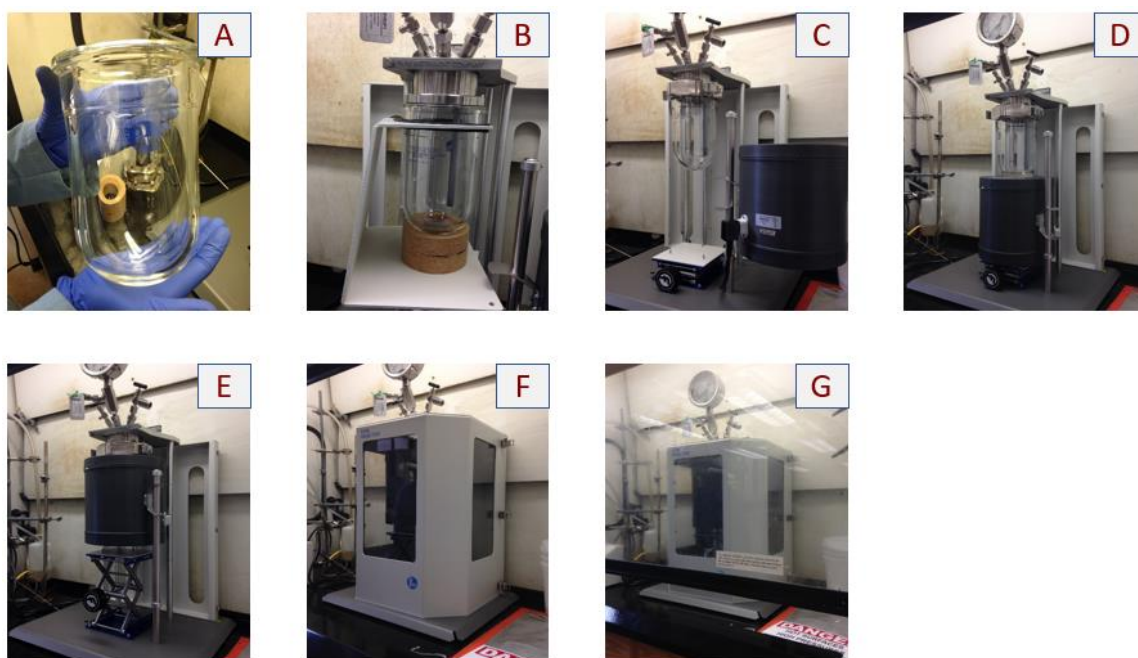


Figure 4: Schematic depiction of the autoclave reactor. (A) Pressure volume vessel used to accommodate the custom fabricated autoclave reactor vessel inserts; (B) Pressure volume vessel on a metal stand. The metal stand is used to stabilize the vessel while loading and unloading the samples; (C) Heating mantle swiveled to the side to allow easy loading and unloading; (D) The heating mantle lowered to quickly observe the vessel; (E) The heating mantle in place; (F) The autoclave protective shield in place; (G) Fume hood lowered for additional safety.

Overloading a pressure vessel is potentially hazardous. Abnormally high pressures can rapidly develop when a liquid is heated in a closed vessel if adequate head-space is not available to accommodate the expansion of the liquid. This could be a problem when dealing with water given that the volume of water may increase by a factor of three when heating from room temperature to a critical point at 374°C. The maximum allowable water loading for the autoclave reactor vessel was calculated using the equation 3, as specified in the autoclave reactor manual.

MAWL = Maximum allowable water loading

$$MAWL = \frac{0.9 \text{ (vessel volume)}}{\text{volume multiplier at maximum temperature}} \dots (3)$$

$$\text{Volume Multiplier} = 1.4$$

$$MAWL = \frac{0.9 \text{ (1500mL)}}{(1.4)}$$

$$\mathbf{MAWL = 964 \text{ mL}}$$

The volume multiplier for water is found in the Parr Instrument Company Document No. 230M: “Safety in the Operation of Laboratory Reactors and Pressure Vessels.”[28]

To test the seals as well as to ascertain the heating rate and pressure values of the autoclave reactor vessel, 500 mL of water was heated using the low heating setting to 100°C. This volume was selected as it is significantly less than the maximum allowable water loading. As observed in figure 5A below, it takes about 45 min to heat water from 25°C to its boiling point of 100°C. The 500 mL water was further heated from 100°C to the recommended 150°C as seen in figure 6A to test the pressure. A temperature of 150°C comes close to modeling post-extraction conditions at most SAG-D sites, while being below the maximum operating pressure of the autoclave reactor as specified by the manufacturer. Ramping to the

desired temperature with a 500 mL volume of water required a duration of 70 min. The vessel then maintained at a pressure of 69 kPa for about 2 h before the test was terminated.

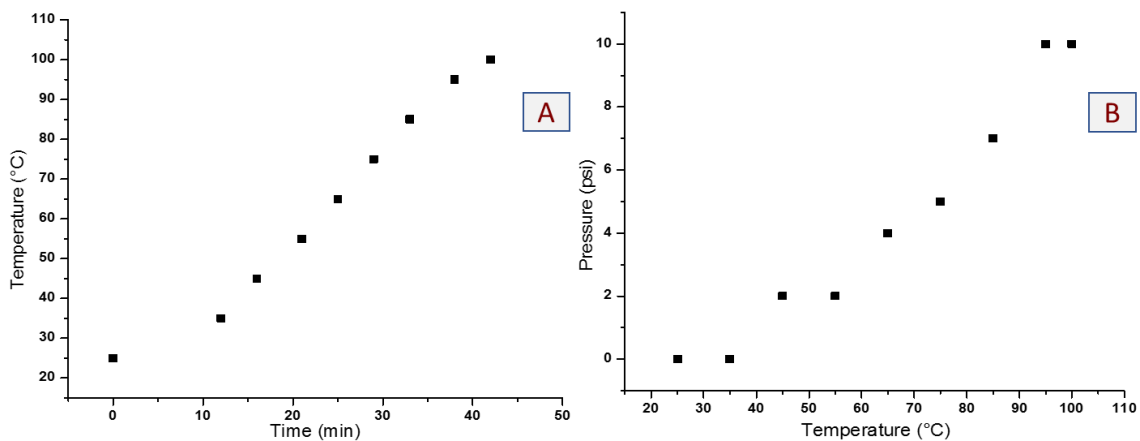


Figure 5: Plots for commissioning of the autoclave reactor with deionized water at different temperatures and pressures. The autoclave vessel is filled with 500 mL of water. (A) Temperature *versus* time for heating water from 25°C to 100°C; (B) Pressure *versus* temperature for heating water from 25 to 100°C.

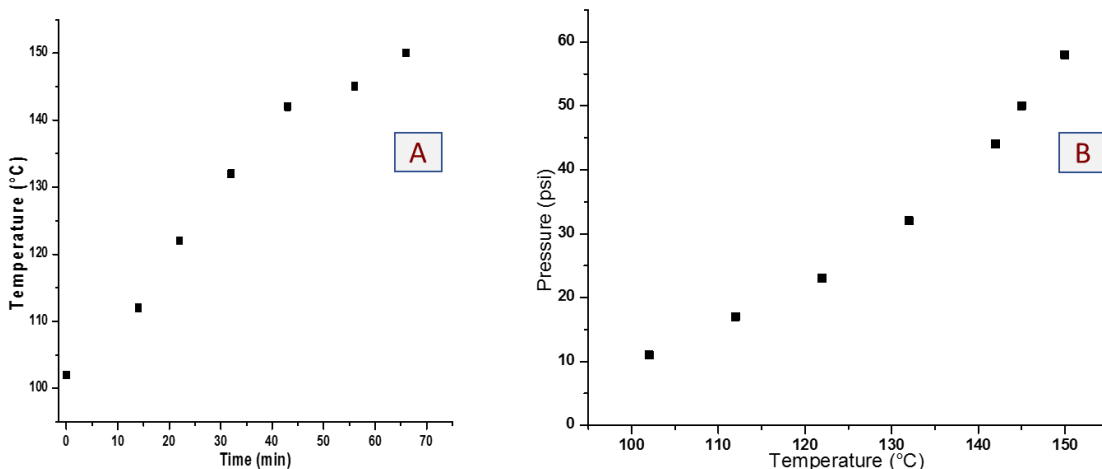


Figure 6: Plots for commissioning of the autoclave reactor with deionized water at different temperatures and pressures. The autoclave vessel is filled with 500 mL of water (A) Temperature *versus* time for heating water from 100°C to 150°C. (B) Pressure *versus* temperature for heating water from 100°C to 150°C.

In a second experiment, 500 mL of water was heated continuously from 21 to 180°C using the low heating setting. The initial data point seen in figure 7A does not fit the trend due to the heat initially absorbed by the vessel and thermal jacket. After 148 min, a maximum temperature and maximum pressure were recorded at 180°C and 917 kPa, respectively (Fig. 7A-B). The heating rate was found to be ca. 1.1°C/min. It is worth noting that these heating rates are not linear, but provide a rough estimate of temperature ramps accessible within this system. It is further important to note the total volume available for expansion is about 1000 mL given that the autoclave reactor vessel's total volume is 1500 mL.

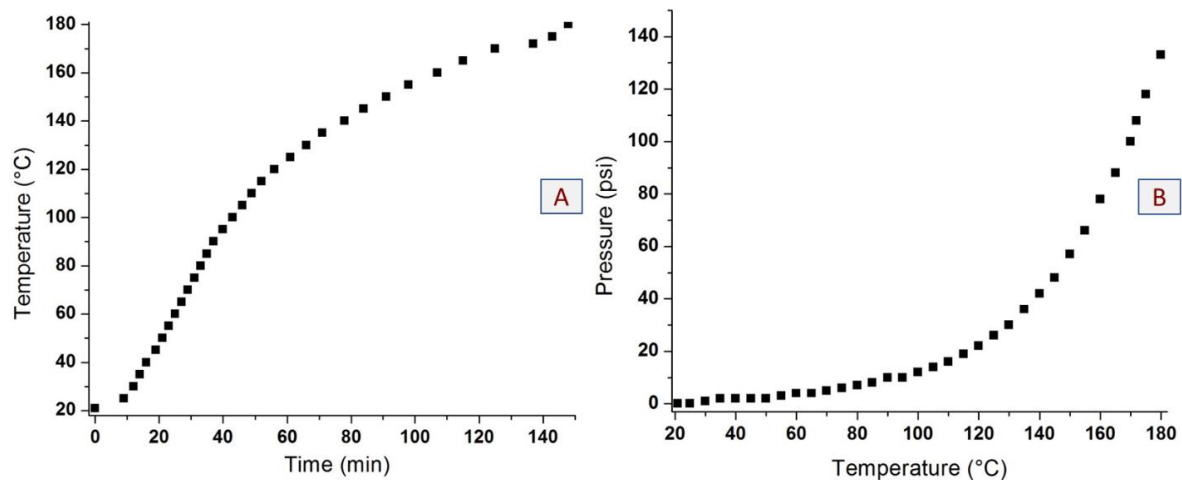


Figure 7: Plots for commissioning of the autoclave reactor with deionized water at different temperatures and pressures. The autoclave vessel is filled with 500 mL of water. (A) Temperature *versus* time for heating water from 21 to 180°C. (B) Pressure *versus* temperature for heating water from 21 to 180°C.

Furthermore, the amount of water was reduced by half (250 mL) to determine the effect on heating rate and pressure. The 250 mL of water was heated still using the low heating setting from 22 to 180°C. It was noticed that a small pressure drop of about 62.1 kPa occurred due to greater volume of 1250 mL in the autoclave reactor vessel available for expansion. The maximum temperature of 180°C occurred after 134 min, whereas a maximum pressure of 862 kPa was reached after 128 min, both represented in figures 8A and 8B. The heating rate at this volume of 250 mL was found to be about 1.2°C/min.

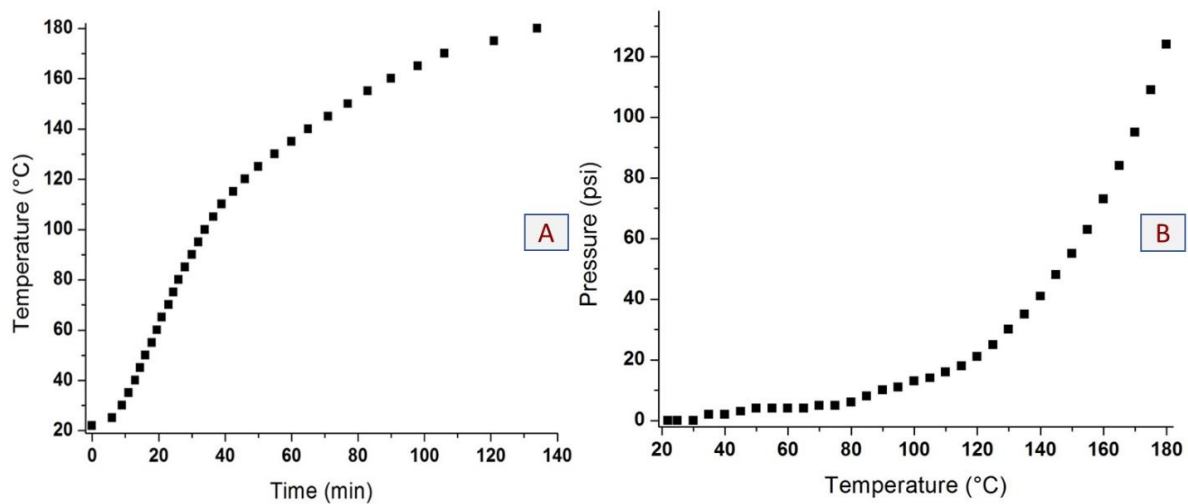


Figure 8: Plots for commissioning of the autoclave reactor with deionized water at different temperatures and pressures. The autoclave vessel is filled with 250 mL of water (A) Temperature *versus* time for heating water from 22 to 180°C. (B) Pressure *versus* temperature for heating water from 22 to 180°C.

The same test was performed with 250 mL volume of water using the reactor's high heating setting. The water was heated from 21 to 175°C. The maximum temperature of 175°C as well as the pressure of 731 kPa was reached in only 45 min. The experiment was halted at 170°C, but residual heat continued to warm the vessel to 175°C. The heating rate under these conditions was observed to be 3.4 °C/min.

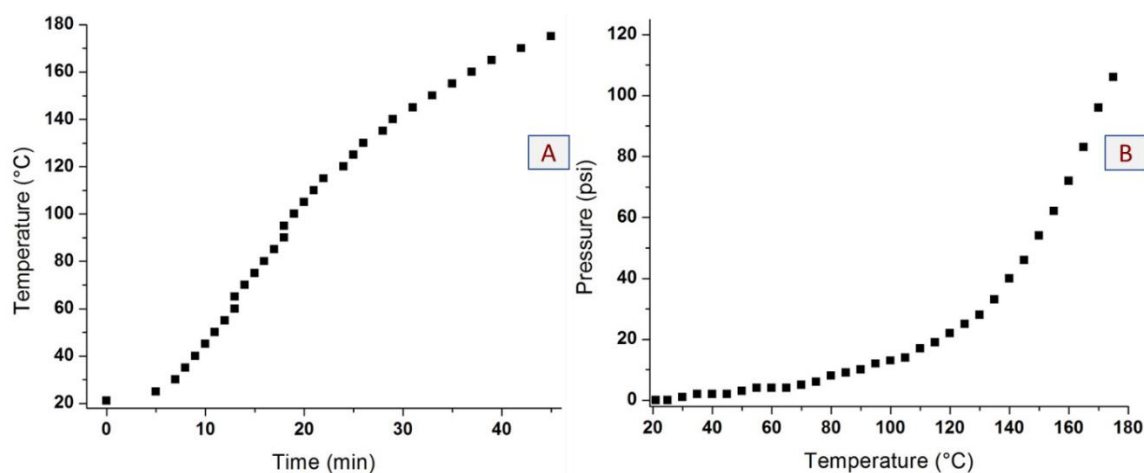


Figure 9: Plots for commissioning of the autoclave reactor with deionized water at different temperatures and pressures. The autoclave vessel is filled with 250 mL of water. (A) Temperature *versus* time for heating water from 22°C to 175°C. (B) Pressure *versus* temperature for heating water from 22°C to 175°C.

It should be noted that 250 mL of water was used as a standard for future experiments as this volume of liquid was heated faster and allowed for a steady pressure to be maintained, while also allowing for a greater volume of headspace (1250 mL). Given the large concentration of volatile fractions in real SAG-D emulsions, the availability of a large headspace is a critical imperative.

2.2 Inserts for Filtration

Custom built inserts were constructed to hold the stainless-steel mesh substrates inside of the autoclave reactor while at the selected temperature and pressure. The custom inserts, designed by Thomas E. O'Loughlin, are made of glass (Fig. 10B). The glass inserts, with inner diameters of ca. 30 mm and varying heights, were custom fabricated in the Department of Chemistry glassblowing facilities to fit inside the 1.5 L autoclave reactor vessel as well as be able to hold ca. 30 mL volume of emulsion for separation. The glass construction makes it possible to visualize the separation process and permits the measurement of (a) flux rates and (b) permeation temperature under realistic process conditions. Figure 10A shows a photograph of constituent elements of the reactor inserts, whereas figures 10B and 10C demonstrates how the parts are assembled. From left to right in figure 10A are two stainless-steel rings with rubber gaskets, the bottom glass insert that collects the dry oil, the top glass insert where the emulsion is introduced, and the O-rings. The glass inserts are secured together with stainless-steel rings (Fig. 10C) and further secured with six screws bolted in a hexagonal pattern to evenly distribute pressure across the membrane and prevent leakage at high ambient autogenous pressures.



Figure 10: Digital photographs of the filtration parts and how they are assembled for deployment under high-pressure and high-temperature conditions.

In short, these experiments provide detailed insight into the behavior of glass inserts due to changes in available volume for expansion. They further demonstrate the importance of using an autoclave reactor to replicate real world separation applications. Figure 11 depicts digital photographs of an initial trial for separating an oil/water SAG-D emulsion. Chapter 3 will further describe the optimization of the separation of emulsions across nanostructured membranes using this apparatus.

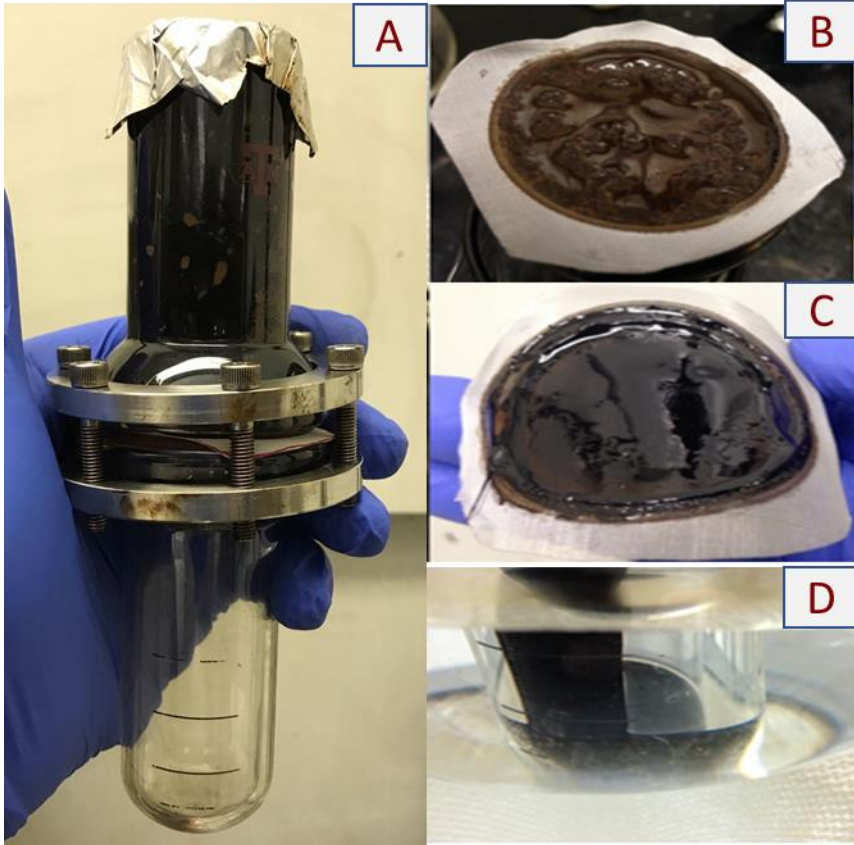


Figure 11: Digital photographs acquired before and after separation of the emulsion. (A) Hydrated bitumen in the top glass inert. The brown coloring is characteristic of the presence of water, which contains soil debris. (B) Digital photograph of the top of the top of the membrane containing retained water with soil debris. (C) Digital photograph of the bottom of the membrane. The black color is characteristic of permeated oil. (D) The permeated oil is darker in color as compared to the original emulsion.

CHAPTER III

CHARACTERIZATION OF MEMBRANE STRUCTURE AND FUNCTION

3.1 Growth of ZnO Tetrapods

The use of ZnO nanotetrapods as the primary building blocks for constructing membranes to engineer the separation of SAG-D water/heavy-oil emulsions was motivated by two central hypotheses:

1. The sharp thorn-like structure of the ZnO tetrapods will bring about the nanoscale texturization of surfaces, thereby rendering metallic meshes hydrophobic and facilitating the use of orthogonal wettability to separate liquids with disparate surface tensions [9].
2. The geometry of the nanostructures precludes close-packing thus creating a porous network through which liquid that wets these structures will permeate.

A scalable method used for the generation of ZnO tetrapods was developed based on the rapid oxidation of Zn foils in air [29]. The zinc metal sheets were cut into small substrates that were ca. 3 mm x 3mm in size (Fig. 12A). The zinc substrates were then placed onto a boat like stainless-steel mesh and then placed within a 1" diameter quartz tube, which was then placed within a tube furnace (Lindburg/BlueM) [30]. The substrates were heated at a rate of 43°C/min until a maximum temperature of 950°C was attained (Fig. 13). The furnace was then held at 950°C for 1 min and then allowed to cool. Figure 14 depicts the thermal ramping profile used to grow ZnO nanotetrapods. Figure 12B shows a digital photograph of ZnO powders collected after the substrates were heated for 1 min at 950°C.

In order to prepare membranes in large-area formats, large amounts of ZnO are required. An estimated 65 g of ZnO was prepared to facilitate the preparation of at least 60 membranes. The loading of ZnO on the membranes was systematically varied. To guarantee the phase purity of the ZnO, the prepared materials were evaluated by X-ray diffraction. Figure 15 shows a representative indexed X-ray diffraction pattern. The morphology of the ZnO tetrapods was evaluated by scanning electron microscopy (SEM).

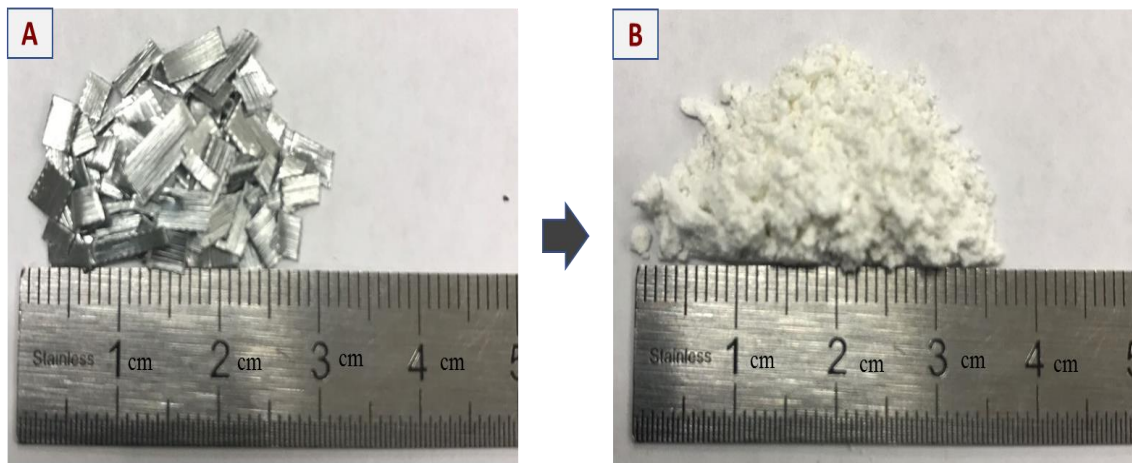


Figure 12: (A) Digital photograph of zinc metal substrates and (B) Powders of ZnO collected after the substrates were heated for 1 min at 950°C.

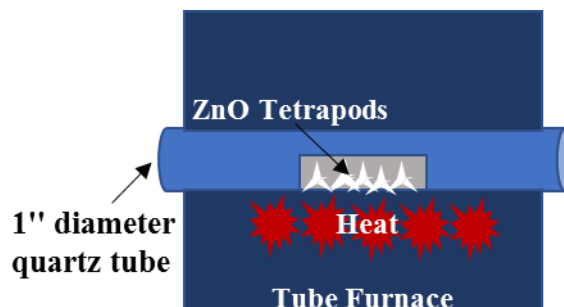


Figure 13: Schematic representation of the apparatus used for generation of ZnO tetrapods.

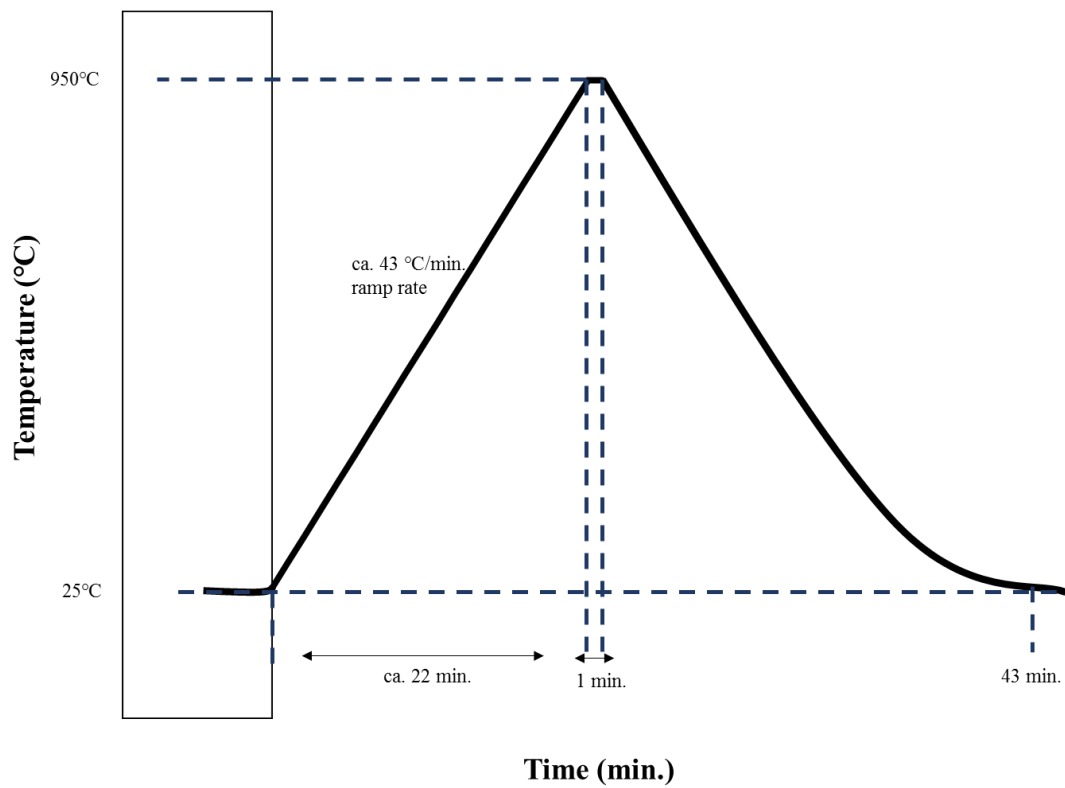


Figure 14: Thermal ramping profile used to grow ZnO nanotetrapods.

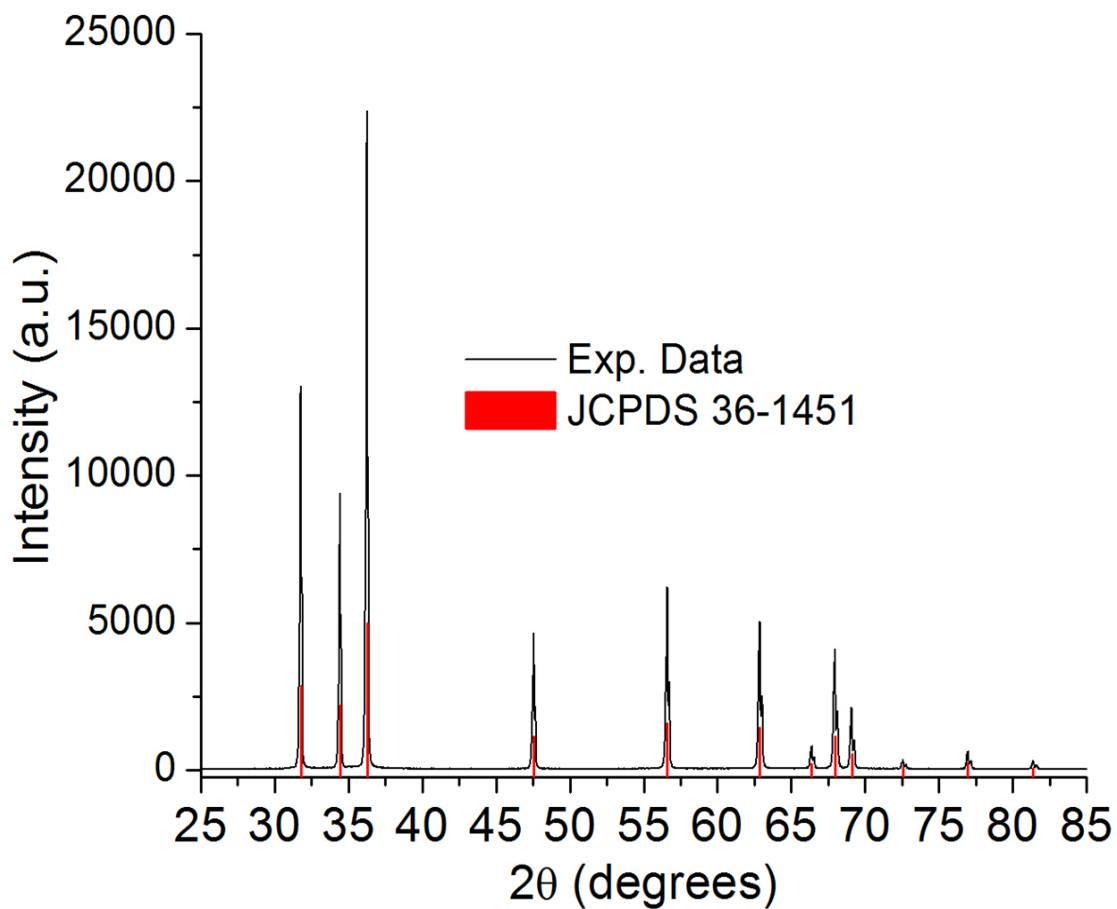


Figure 15: Representative X-ray diffraction pattern. Plot reproduced with permission from Thomas O’Loughlin [9]. All reflections can be matched with the reflections of zincite ZnO in the hexagonal phase (Joint Committee on Powder Diffraction Standards 36-1451).

3.2 Preparation of membrane by spray coating of ZnO onto stainless steel mesh

After the ZnO nanostructure was synthesized, the crystalline nanostructures were then dispersed in 2-propanol to obtain dispersions with a concentration of ca. 20 mg/mL. The dispersion was then spray coated onto stainless steel mesh substrates with a variety of pore sizes (McMaster-Carr) using a Master airbrush with a nozzle diameter of 0.5 mm, and an air compressor with output pressure of 310.3 kPa. To facilitate the removal of solvent during the coating process, the stainless steel meshes were held at a temperature of ca. 120°C. Using a modified Stöber method, a layer of SiO₂ was additionally deposited to optimize the adhesion and the mechanical resilience of the ZnO nanostructures [31]. The deposition of an amorphous SiO₂ shell represents a critically important step because nanostructures that are only adsorbed are readily sloughed. To deposit a SiO₂ shell, tetraethylorthosilicate (TEOS) was used as the precursor. The solution spray coated on the stainless-steel mesh comprised a mixture of ethanol (80 vol.%), deionized water (18.5 vol.%), an aqueous solution of NH₄OH (1 vol.% of 28—30%), and TEOS (0.5 vol.%). The substrates were held at a temperature of ca. 120°C during the spray coating of the TEOS solutions to facilitate solvent removal. Figures 16A—F indicate the mesoscale porosity defined by the interconnected network of ZnO nanotetrapods that span across the pores of the metal meshes. The SEM image in Figures 16F show that the nanotetrapods define a “bed of nails”.

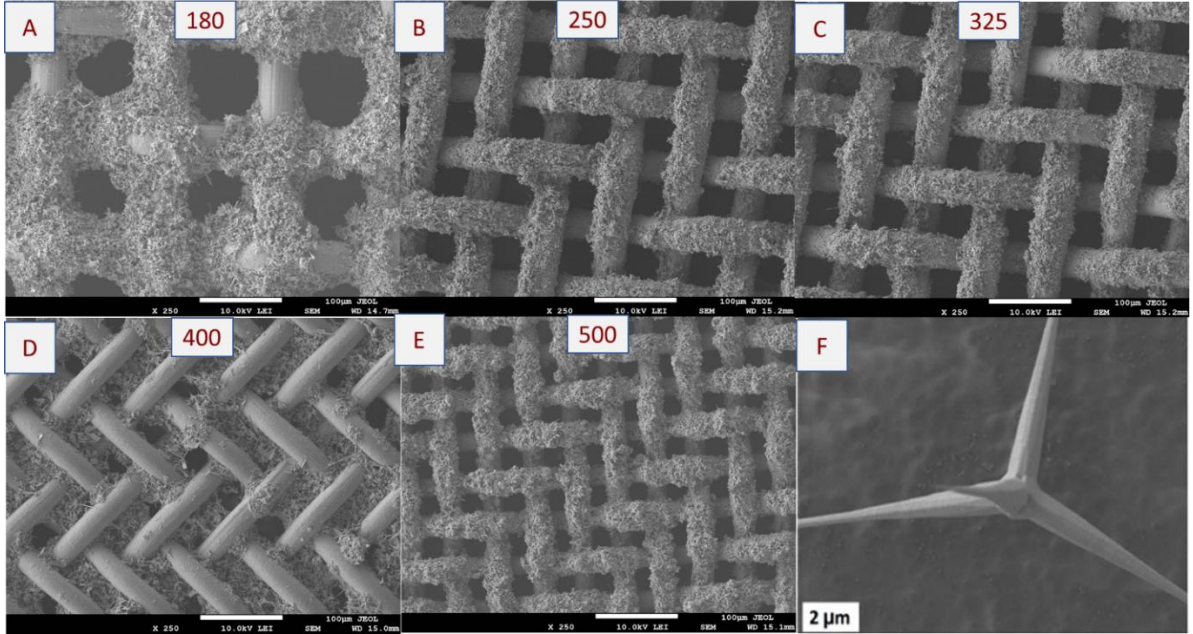
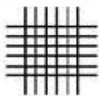
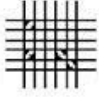






Figure 16: SEM images depicting the multiscale textured metal meshes modified by the deposition of ZnO nanotetrapods at various magnifications. All samples shown have a ZnO loading of ca. 7.0 mg/cm^2 (A) 180-gauge textured metal mesh with a pore size of ca. $84 \text{ }\mu\text{m}$; (B) 250-gauge textured metal mesh with a pore size of ca. $61 \text{ }\mu\text{m}$; (C) 325-gauge textured metal mesh with a pore size of ca. $43 \text{ }\mu\text{m}$; (D) 400-gauge textured metal mesh with a pore size of ca. $38 \text{ }\mu\text{m}$; (E) 500-gauge textured metal mesh with a pore size of ca. $30 \text{ }\mu\text{m}$; (F) a single ZnO tetrapod. Panel (F) is reproduced with permission from [9]. Copyright 2017 John Wiley and Sons

To test the separation efficiency for this work, different stainless steel meshes with varying pore sizes were used. The meshes include 180-gauge, 250-gauge, 325-gauge, 400-gauge mesh, and 500-gauge mesh corresponding to pore sizes of ca. $84 \text{ }\mu\text{m}$, $61 \text{ }\mu\text{m}$, $43 \text{ }\mu\text{m}$, $38 \text{ }\mu\text{m}$, and $30 \text{ }\mu\text{m}$, respectively (Fig. 17). Figure 16 depicts SEM images of the different mesh sizes with a ZnO loading of ca. 7.0 mg/cm^2 in each case. The TEOS loading as well as the associated parameters were varied to obtain good adhesion as verified by the American Society for testing of Materials (ASTM) tests D3359 and D2197. The ASTM D3359 test, is the standard test method for measuring adhesion by tape test. Adhesion is tested by using a tool to scratch through the coating, making a grid. Tape is then applied and removed and the

adhesion is given rating based on the percent of the removed material. Table 1 shows the rating scale for tape test in ASTM D3359. The ASTM D2197 test on the other hand is a standard test method for adhesion of organic coatings by scrape adhesion. Scrape adhesion of coatings is tested by sliding the sample under a U-shaped tip and adding weight until the coating breaks through the underlying substrate.

Table 1: Rating scale for tape test in ASTM D3359. Table reproduced with permission from ASTM International [32].

Classification of Adhesion Test Results		
Classification	Percent Area Removed	Surface of Cross-Cut Area From Which Flaking has Occured for Six Parallel Cuts and Adhesion Range by Percent.
5B	0% None	
4B	Less Than 5%	
3B	5-15%	
2B	15-35%	
1B	35-65%	
0B	Greater Than 65%	

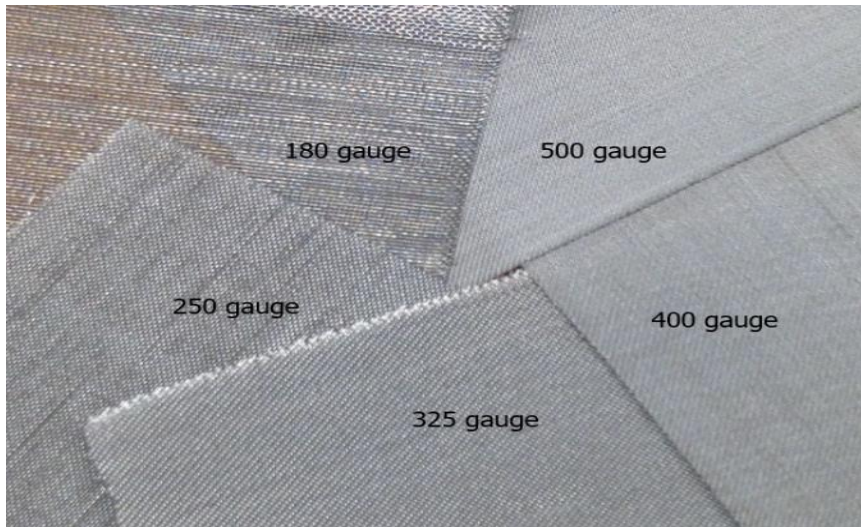


Figure 17: Digital photograph of meshes used for the investigation

3.3 Characterization of SAG-D emulsions

As detailed in chapter 1, SAG-D emulsions were reconstituted. Given the viscous nature of the Canadian Oil Sands, the SAG-D method is used. Upon extensive mechanical agitation, the extracted liquid is a reconstituted emulsion of oil and water.

Optical microscopy results as depicted in Figure 18 show that SAG-D emulsions have a complex hierarchical structure with oil droplets dispersed within a continuous water phase containing water droplets that further contain asphaltene residues. The nature of these reconstituted emulsion make is very hard for the oil and water to separate, as higher temperatures are required to crack the emulsion.

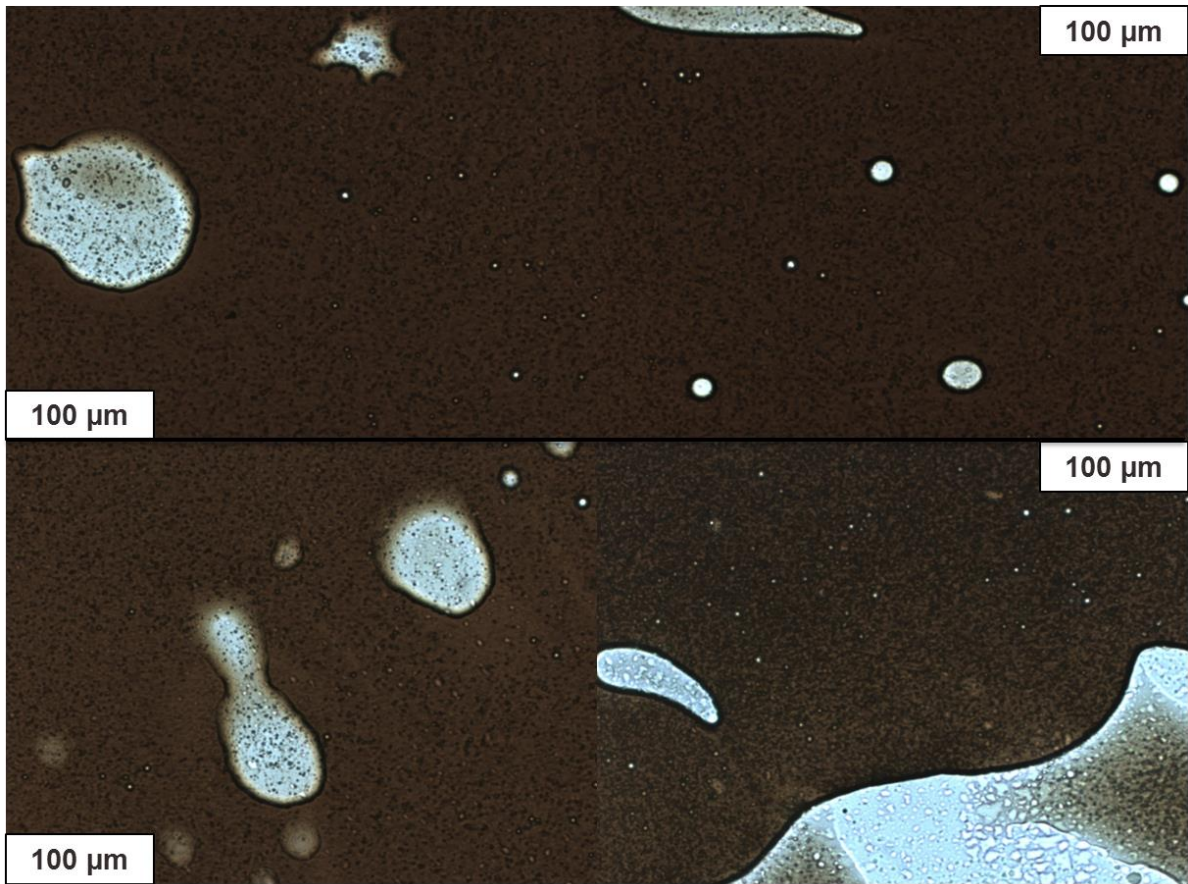


Figure 18: Optical microscopy image of a reconstituted bitumen emulsion that is untreated (not permeated). The lighter regions correspond to water droplets. Note that there are also some oil droplets embedded within the water droplets. The water content is estimated to be ca. 30 vol. % in this sample as per Dean-Stark's method. Darker solid particles are asphaltene residues.

3.4 Evaluation of the efficacy of hierarchically textured membranes

A key objective for engineering the efficacious separation of SAG-D emulsions was to develop membranes capable of separating emulsions under realistic process conditions. Consequently, the research effort has focused on examination of the (a) the permeation temperature; (b) the separation efficacy; and (c) the flux rate as a function of the pore size and ZnO loading under high-temperature and high-pressure conditions is critical.

As detailed in Chapter 2, a custom testing apparatus that can operate at temperatures of 200°C and pressures of up to 900— 1000 kPa was designed for this purpose. The system was filled with water up to 250 mL and heated to temperatures of 150 — 200°C. The autogenous pressure from boiling of water reached 731 kPa. Figure 19 depicts the process flow beginning from the coating of the metal meshes to the separation of emulsions under conditions of high temperature and pressure. The permeation temperature was recorded as soon as visible bitumen was seen permeating through the membrane in the autoclave.

The key parameter is of course the separation efficiency. Dean-Stark's method along the help of optical microscopy has been used to evaluate the water content within the permeated heavy oil fractions. For samples with water content less than 1 vol.%, Karl Fischer titration was used instead. In the Dean-Stark's method for determination of water content, given the viscous nature of the permeated bitumen, a solvent (toluene) was mixed with the bitumen and then boiled. 10 mL of toluene was added to the permeated bitumen. As the solvent, along with bitumen boiled using a heating mantle, the solvent evaporated and then condensed into a calibrated trap, where the quantity of water present in the bitumen was calculated (Fig. 20). To obtain statistically meaningful results, a minimum of 3 membranes with the same pore size as well as ZnO loading were tested.

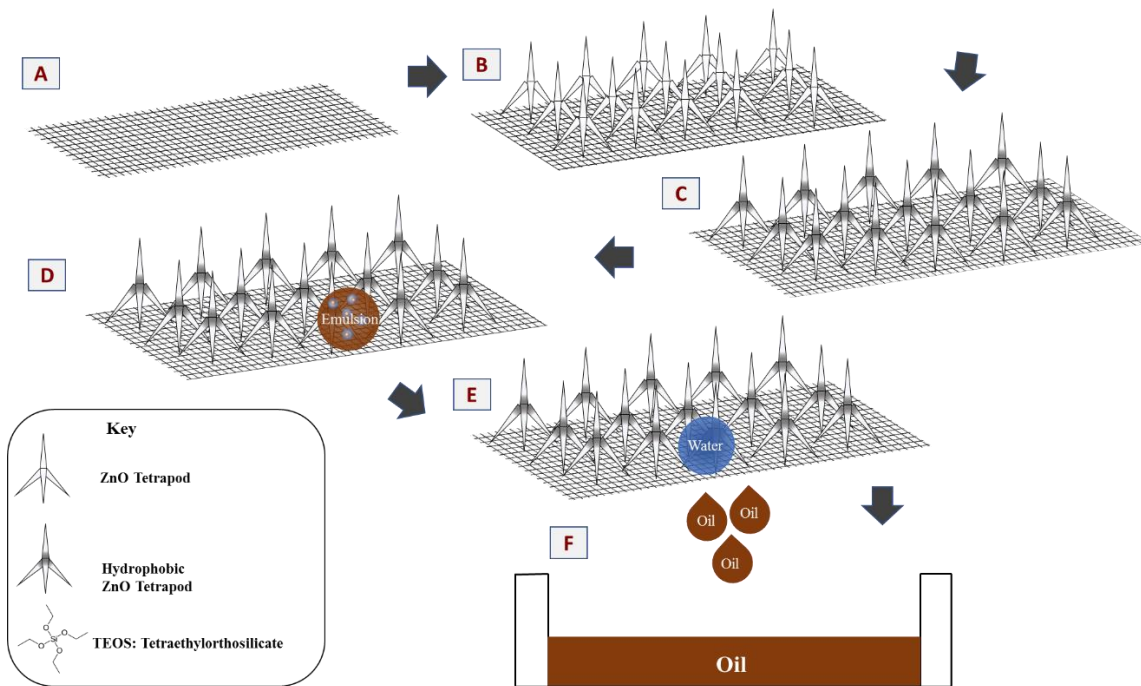


Figure 19: Schematic representation of the separation process; (A) Stainless steel mesh used; (B) ZnO tetrapods spray deposited on stainless steel mesh; (C) Functionalization of stainless steel mesh using TEOS; (D) Application of emulsion to functionalized and ZnO-coated stainless-steel mesh. The brown coloration of the emulsion droplet represents the oil, whereas the blue area is the water. It can further be seen that in the water, there are some residual oil; (E) Separation of water and oil; (F) Collection of oil.

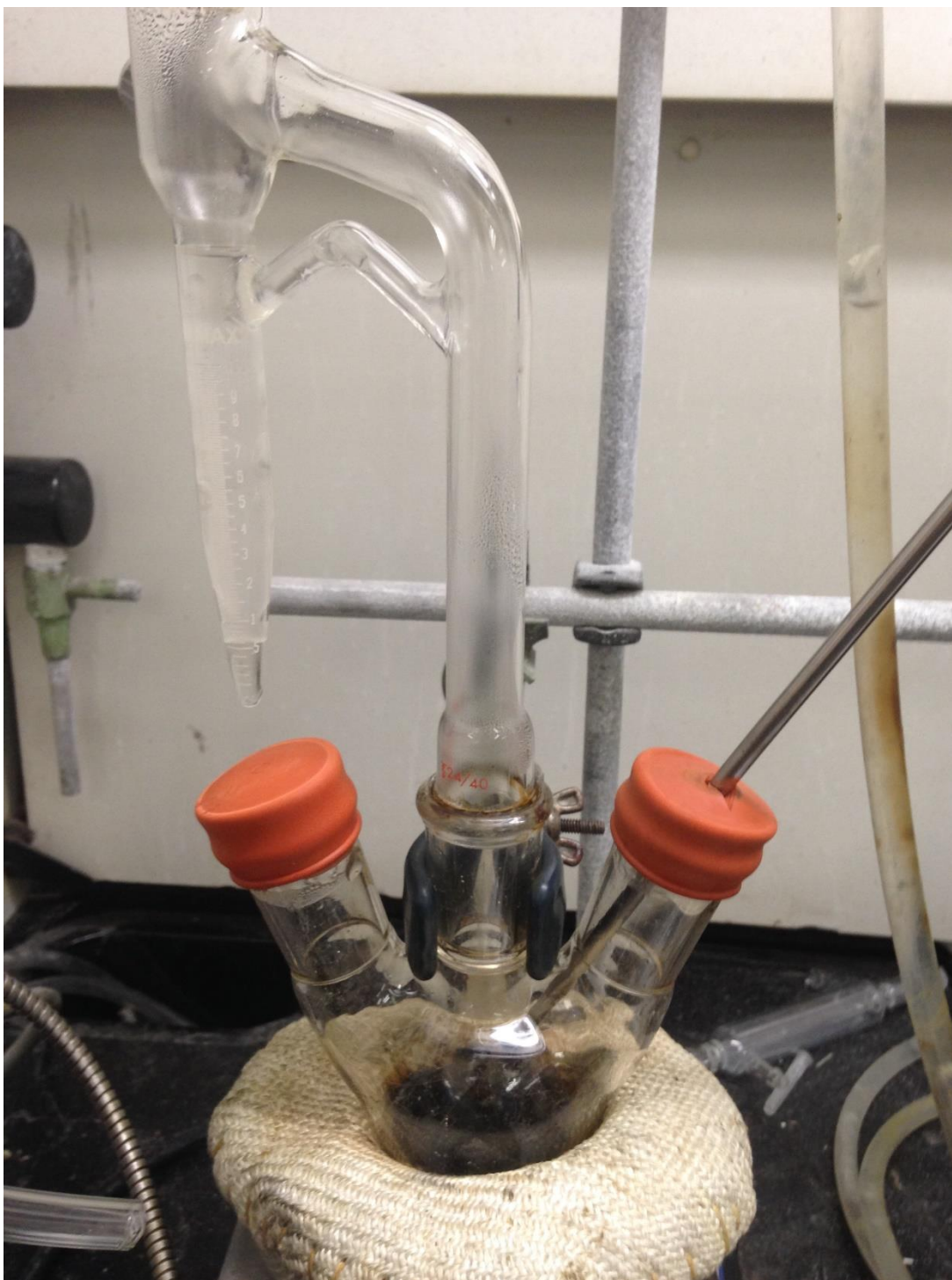


Figure 20: Digital photograph of the Dean-Stark placed above a round-bottom flask. The metal rod in the round-bottom flask is the thermocouple. The round-bottom flask is placed on the heating mantle used to boil the bitumen and solvent mixture. The black color in the round-bottom flask is the boiling mixture of the bitumen and the solvent. The liquid in the Dean-Stark is the condensed water and solvent mixture.

3.5 Membrane Performance

For meshes characterized by larger pore sizes, 180 and 250-gauge corresponding to pore sizes of 84 μm and 61 μm respectively, it was observed that most of the oil started penetrating through the membrane at low temperatures and low pressures. As discussed in Section 3.3, as a result of the complex nature of the emulsions, water droplets entrained within oil droplets will permeate through if a separation is engineered at low temperatures based on surface tension alone. The fundamental issue herein is thus that a temperature of 140°C is required to crack the emulsions and thus ideally permeation should occur only above temperatures where the concentric nature of the emulsions has been disrupted. In other words, permeation at low temperatures will inevitably yield samples with high degrees of water contamination since only free water can be separated under these conditions. Notably, the use of high temperatures is further necessary given the operating conditions under which SAG-D emulsions are extracted and handled. Figure 21 depicts that smaller dimensions necessitate the use of higher temperature for permeation of the bituminous phase. Likewise, with increase ZnO loading, higher permeation temperatures were required to permeate the bitumen providing opportunities for reducing water content.

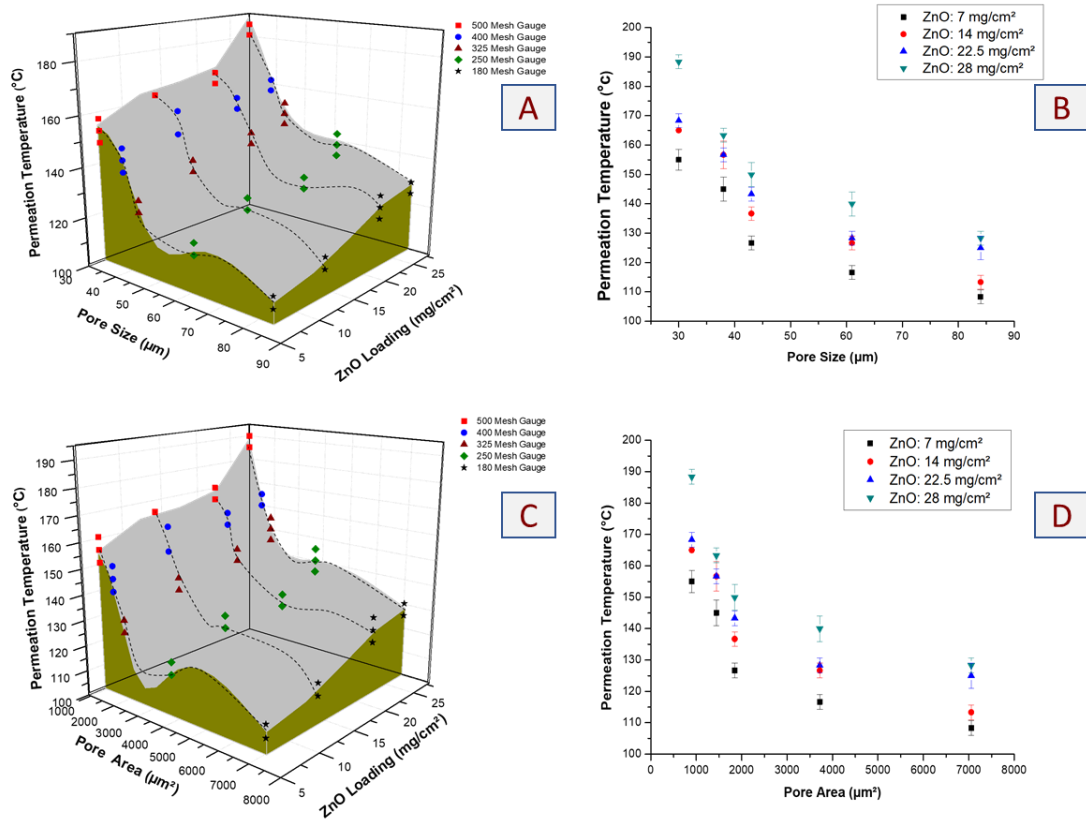


Figure 21: (A) 3D Plot depicting the variation of the permeation temperature behavior as a function of the pore size and ZnO loading on the membrane. (B) 2D plot of the permeation temperature as a function of the pore size at different ZnO loadings. (C) 3D plot depicting the variation of the permeation temperature behavior as a function of the pore area and the ZnO loading on the membrane (D) 2D plot of the permeation temperature as a function of the pore area at different ZnO loadings.

The critical parameter for technological viability is of course the separation efficiency. By using the Dean-Stark method, the amount of water that permeated through the different membranes was quantified. The water content of a hydrated bitumen emulsion, which is the precursor used in all of the experiments, is 30 vol. %. The water content recovered in the permeate is a function of the permeation temperature and thus also the pore size and ZnO loading. Membranes with larger pore dimensions and relatively low ZnO loadings, such as 180 and 250-gauge meshes with ZnO loadings of 7 mg/cm² permeate 18.5 mL and 15.7 mL amount of water, respectively. While the water content is substantially reduced from the hydrated emulsions, most of the water content eliminated is free water and emulsified water droplets are largely permeated given the low permeation temperature of 117 and 127°C, respectively. In stark contrast, the 500-gauge mesh with a ZnO loading of 22.5 mg/cm² yielded a permeate with a water content of 0.6 vol. %. Figure 22 depicts plots of the water purity as a function of the mesh size and ZnO loading.

The permeate fractions have been further examined by optical microscopy. In order to perform the analysis, ca. 1 mL of the permeated fraction was collected. Using a syringe, the permeated fraction was deposited onto a thin microscope slide. The sample was then observed under the Olympus microscope. Figures 18, 23-26 depict optical microscopy images of the permeate fractions. Water and oil are clearly distinguishable and analysis of multiple cover slip samples indicates trace amounts of water. Karl—Fisher titration results suggest a water content of 0.6 vol. % for the permeate recovered using a 400-gauge membrane with a pore size of 38 μm and ZnO loading of 28 mg/cm².

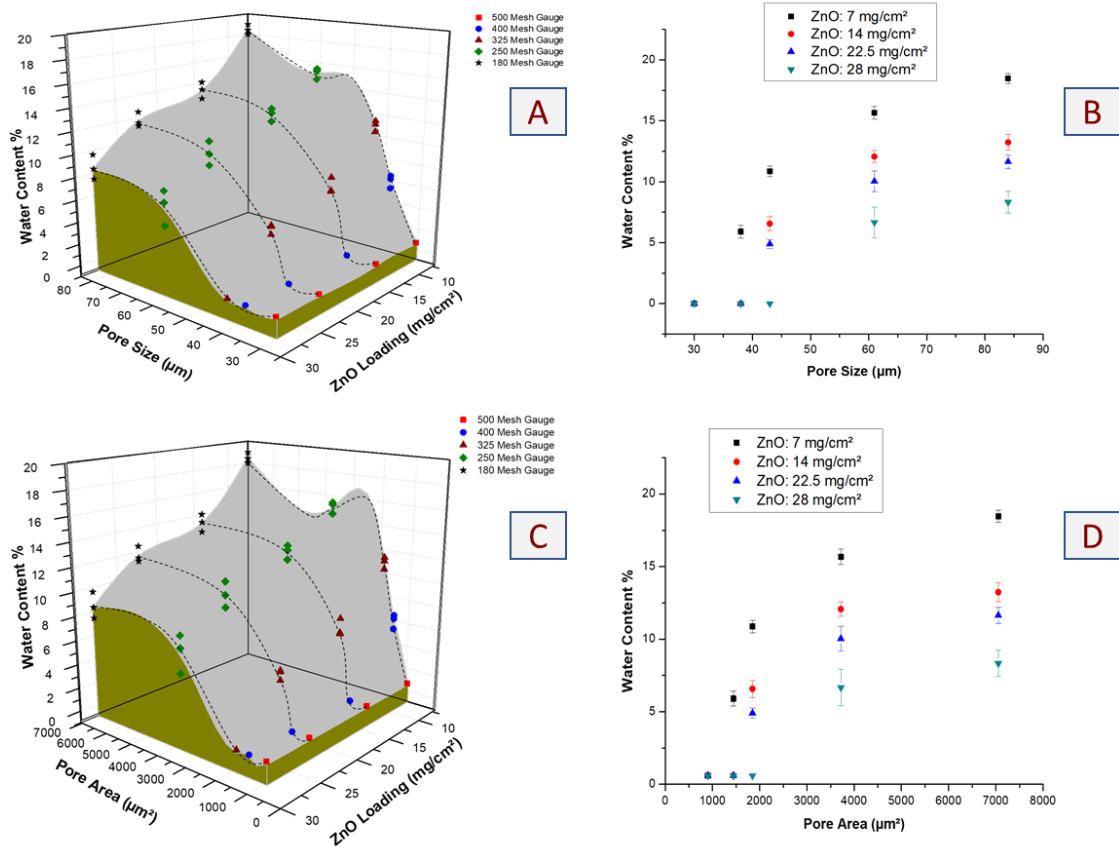


Figure 22: (A) 3D Plot depicting the variation of the water content percentage as a function of the pore size and ZnO loading on the membrane. (B) 2D plot of the water content percentage as a function of the pore size at different ZnO loadings. (C) 3D plot depicting the variation of the water content percentage as a function of the pore area and the ZnO loading on the membrane. (D) 2D plot of the water content percentage as a function of the pore area at different ZnO loadings.

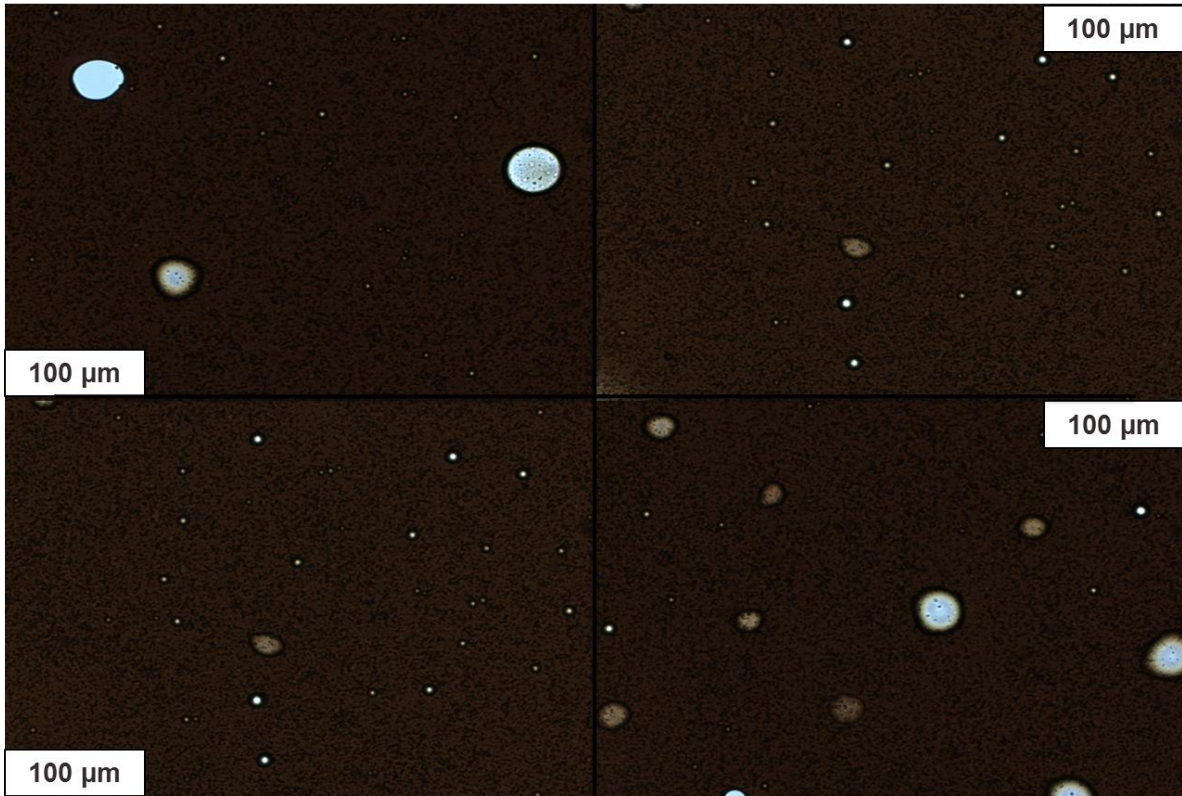


Figure 23: Optical microscopy of a reconstituted bitumen emulsion that permeated through a 250-gauge mesh with a pore size of 61 μm . The lighter regions correspond to water droplets. Note that there are also some oil droplets embedded within the water. Water content is ca. 14 vol. % in this sample as per Dean-Stark's method. Darker solid particles are asphaltene residue.

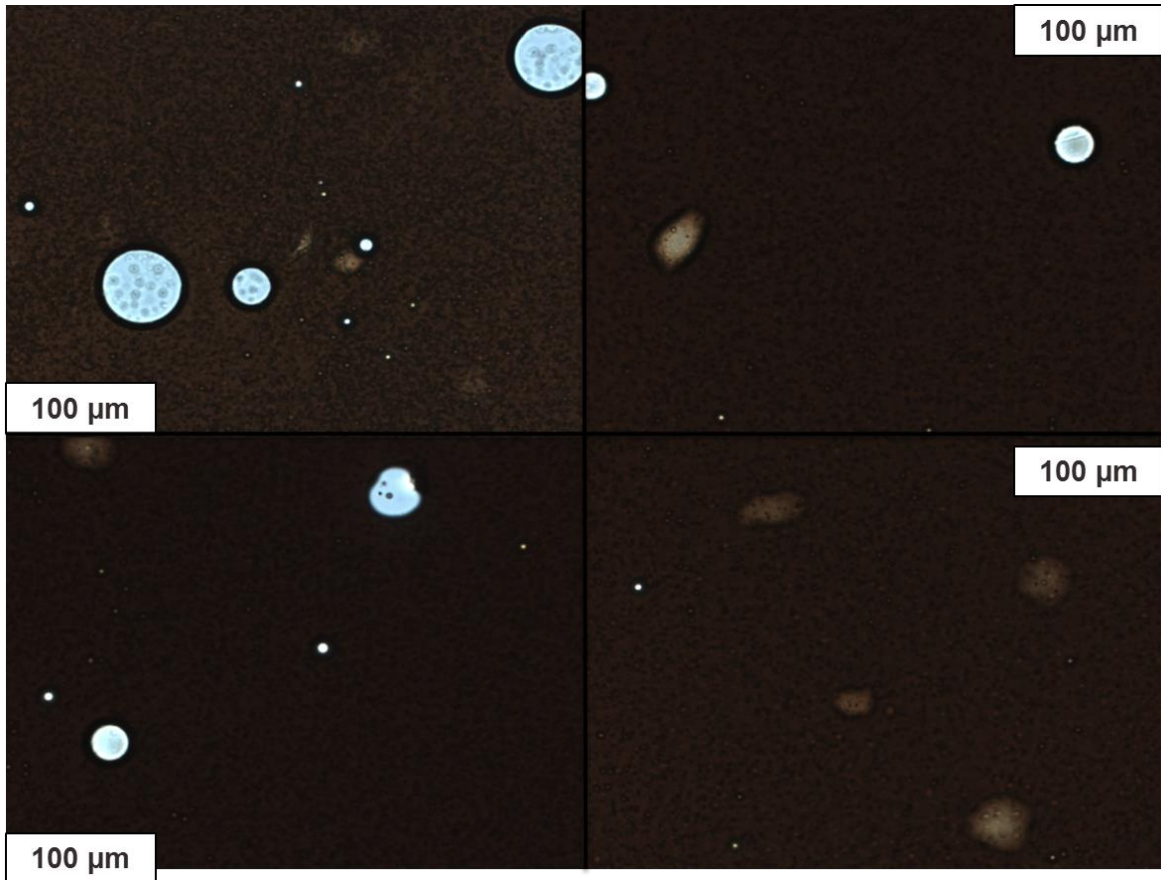


Figure 24: Optical microscopy of a reconstituted bitumen emulsion that permeated through a 325-gauge mesh with a pore size of 43 μm . The lighter regions correspond to water droplets. Note that there are also some oil droplets embedded within the water. Water content is ca. 10 vol. % in this sample as per Dean-Stark's method. Darker solid particles are asphaltene residue.

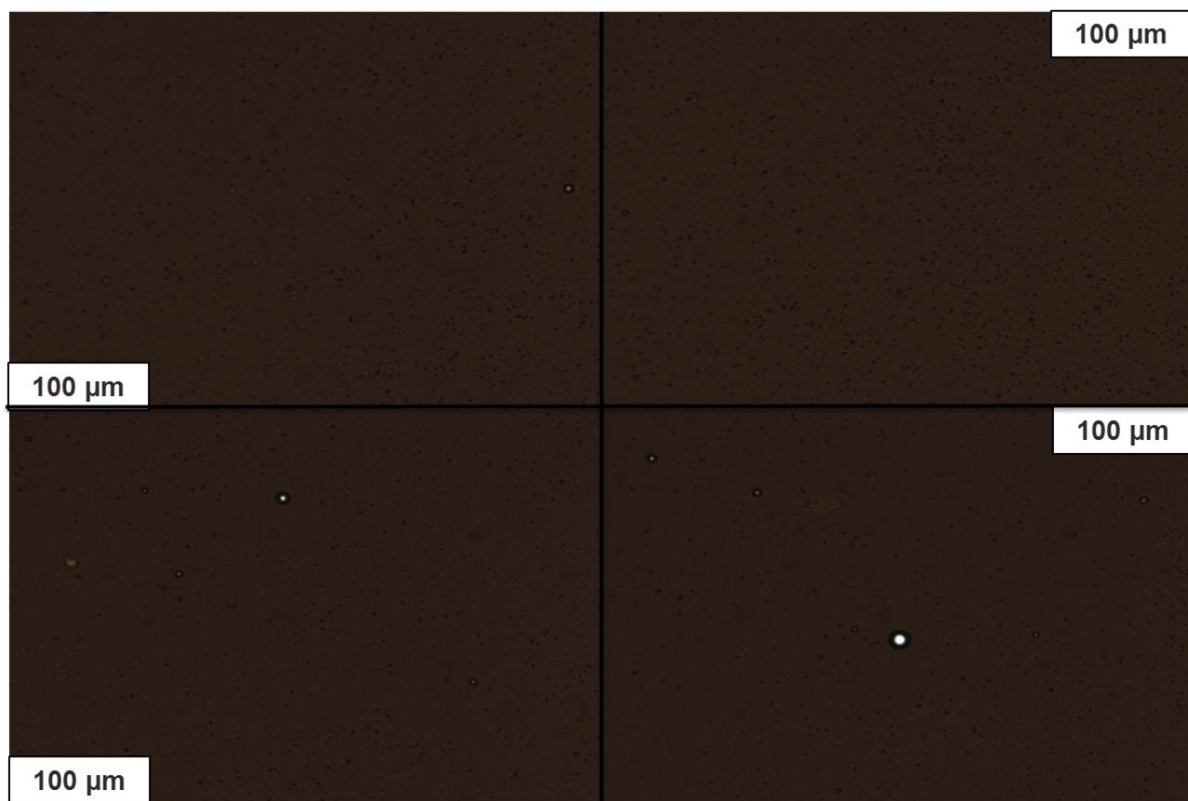


Figure 25: Optical microscopy of a reconstituted bitumen emulsion that permeated through a 400-gauge mesh with a pore size of 38 μm . The lighter regions correspond to water droplets. Note that there are also some oil droplets embedded within the water. Water content is ca. 0.6% vol. % in this sample as per Karl Fisher's titration method. Darker solid particles are asphaltene residue.

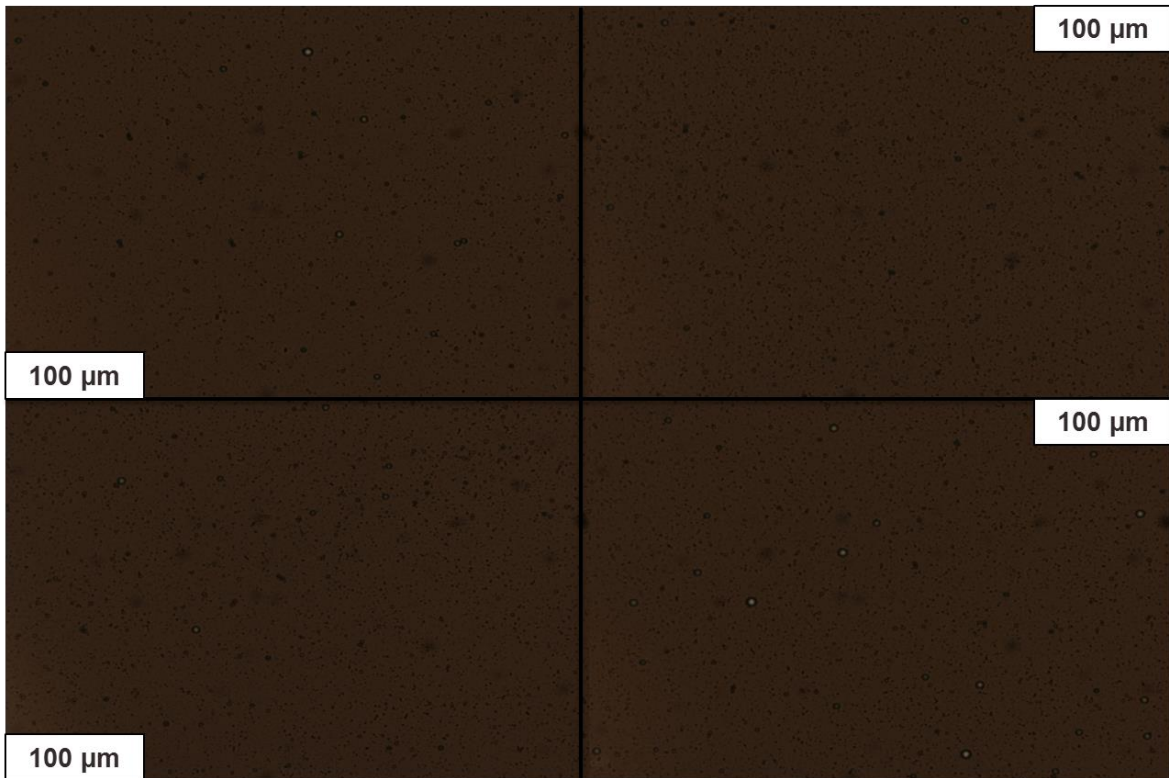


Figure 26: Optical microscopy of a reconstituted bitumen emulsion that permeated through a 500-gauge mesh with a pore size of 30 μm . The lighter regions correspond to water droplets. Note that there are also some oil droplets embedded within the water. Water content is ca. 0.6% vol. % in this sample as per Karl Fisher's titration method. Darker solid particles are asphaltene residue.

For industrial viability, the flux rate is another important parameter. Figure 27 depicts that the flux rate is inversely correlated to water purity. In each instance, the flux rate has been measured at the permeation temperature and it is expected that higher temperatures will enhance the flux rate without compromising purity. For larger pore dimensions and lower ZnO loadings, the flux rate is high (reaching 20 mL/h) despite the relatively low permeation temperatures. In contrast, the flux rate is diminished for smaller pore dimensions and higher ZnO loadings. The decrease in flux rates engendered by increased ZnO loading can be rationalized by the smaller effective pore diameter. For a 500-gauge mesh with a ZnO loading of 28 mg/cm², no permeation is observed up to a temperature of 190°C.

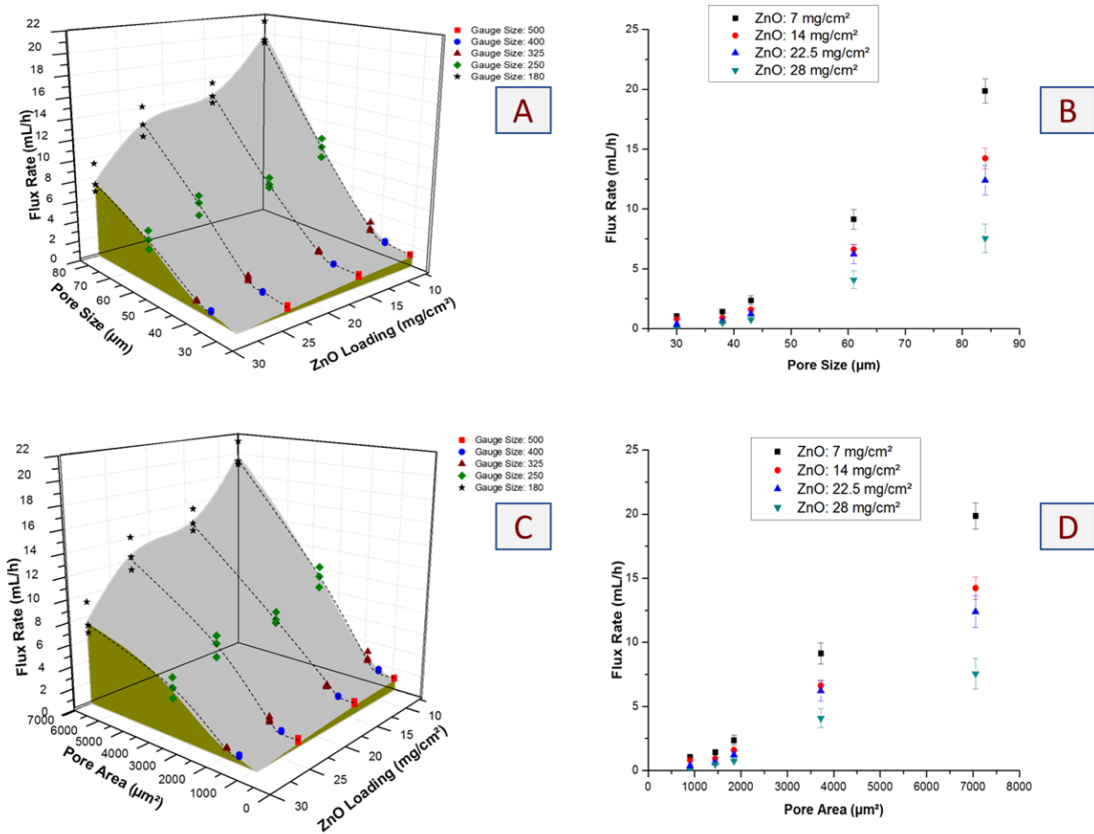


Figure 27: Plots showing the flux rate behavior with respect to the pore size, pore area and also ZnO loadings on the membrane; (A) 3D plot depicting the variation of the flux rate as a function of the pore size and the ZnO loading on the membrane. (B) 2D plot of the flux rate as a function of the pore size at different ZnO loadings. (C) 3D plot depicting the variation of the flux rate as a function of the pore area and the ZnO loading on the membrane (D) 2D plot of the flux rate as a function of the pore area at different ZnO loadings.

CHAPTER IV

CONCLUSIONS AND FUTURE DIRECTIONS

This thesis was successful in developing and evaluating the efficacy of hierarchically textured membranes for the separation of realistic SAG-D emulsions. The commissioning of the high pressure and high-temperature vessel, discussed in Chapter 2, gave us the ability to reproduce industrial conditions for the separation of emulsions on a laboratory scale. On the basis of this work, discussed in Chapter 3, it was concluded that the use of high temperatures was necessary for the separation given the operating conditions under which the emulsions are extracted and handled. Such high temperatures are required to break apart complex emulsions. Based on the results presented in Chapter 3, membranes with small pore sizes are necessary to significantly reduce the quantity of water present in the emulsions. The flux rate also showed a great variance between high and low permeation temperatures as well as high and low ZnO concentrations. Ongoing efforts are focused at simultaneously optimizing the separation efficacy and the flux rate by examining whether high separation efficiencies can be obtained at still higher temperatures.

From an environmental standpoint, the development of a physical means of engineering the separation of emulsions provides an interesting alternative for addressing oil spills in marine environments such as the Deepwater Horizon spill. This separation technique will be very advantageous to the midstream companies, as it will limit the transportation issues that are related with oil and water emulsions.

Although this research shows a great deal of success in the evaluation of membranes, in the industrial world there are some challenges that could be faced. One of the major challenges is the manufacturing of large-area membranes. The separation efficiency with large-area membranes could reduce. The membrane could further be easily fouled by soil and asphaltene debris making the recycling of the membrane challenging [33]. Additional research is needed to explore whether surface functionalization can be used as a means to further optimize the separation efficacy and flux rate [9].

Further research and tests involving the membranes study include reverse phase separation, where instead of making the membrane hydrophobic for the permeation of emulsions, the membranes are made superhydrophilic instead for water to permeate through the membrane and the emulsion is retained [33]. Furthermore, research in embedding catalytic functionality in the membranes is another pathway that could be taken to not just separate the water and oil components of emulsions but to also upgrade the recovered oil in the process.

- [10] S. Wang *et al.*, “Manipulation of surface wettability between superhydrophobicity and superhydrophilicity on copper films,” *ChemPhysChem*, vol. 6, no. 8, pp. 1475–1478, 2005.
- [11] G. a. Horrocks, M. F. Likely, J. M. Velazquez, and S. Banerjee, “Finite size effects on the structural progression induced by lithiation of V₂O₅: a combined diffraction and Raman spectroscopy study,” *J. Mater. Chem. A*, vol. 1, p. 15265, 2013.
- [12] W. M. Haynes, *CRC Handbook of Chemistry and Physics*, 95th ed. CRC Press.
- [13] D. Quéré, “Wetting and Roughness,” *Annu. Rev. Mater. Res.*, vol. 38, no. 1, pp. 71–99, 2008.
- [14] N. J. Shirtcliffe, G. McHale, S. Atherton, and M. I. Newton, “An introduction to superhydrophobicity,” *Adv. Colloid Interface Sci.*, vol. 161, no. 1–2, pp. 124–138, 2010.
- [15] P. Roach, N. J. Shirtcliffe, and M. I. Newton, “Progress in superhydrophobic surface development,” *Soft Matter*, vol. 4, no. 2, p. 224, 2008.
- [16] J. Drelich and E. Chibowski, “Superhydrophilic and superwetting surfaces: Definition and mechanisms of control,” *Langmuir*, vol. 26, no. 24, pp. 18621–18623, 2010.
- [17] J. A. Lee and T. J. McCarthy, “Polymer surface modification: Topography effects leading to extreme wettability behavior,” *Macromolecules*, vol. 40, no. 11, pp. 3965–3969, 2007.
- [18] P. S. Brown, O. D. L. a Atkinson, and J. P. S. Badyal, “Ultrafast Oleophobic – Hydrophilic Switching Surfaces for Antifogging , Self-Cleaning , and Oil – Water Separation,” *Appl. Mater. Interfaces*, 2014.
- [19] Z. Wang, X. Jiang, X. Cheng, C. H. Lau, and L. Shao, “Mussel-inspired hybrid

- coatings that transform membrane hydrophobicity into high hydrophilicity and underwater superoleophobicity for oil-in-water emulsion separation,” *ACS Appl. Mater. Interfaces*, vol. 7, no. 18, pp. 9534–9545, 2015.
- [20] Y. Si *et al.*, “Superelastic and Superhydrophobic Nano fiber-Assembled Cellular Aerogels for Effective Separation of Oil / Water Emulsions,” *ACS Nano*, vol. 9, no. 4, pp. 3791–3799, 2015.
- [21] K. Li *et al.*, “Structured cone arrays for continuous and effective collection of micron-sized oil droplets from water,” *Nat. Commun.*, vol. 4, p. 2276, 2013.
- [22] B. R. Solomon, M. N. Hyder, and K. K. Varanasi, “Separating oil-water nanoemulsions using flux-enhanced hierarchical membranes,” *Sci. Rep.*, vol. 4, p. 5504, 2014.
- [23] J. A. Howarter and J. P. Youngblood, “Amphiphile grafted membranes for the separation of oil-in-water dispersions,” *J. Colloid Interface Sci.*, vol. 329, no. 1, pp. 127–132, 2009.
- [24] M. Takht Ravanchi, T. Kaghazchi, and A. Kargari, “Application of membrane separation processes in petrochemical industry: a review,” *Desalination*, vol. 235, no. 1–3, pp. 199–244, 2009.
- [25] Y. Zhu, D. Wang, L. Jiang, and J. Jin, “Recent progress in developing advanced membranes for emulsified oil/water separation,” *NPG Asia Mater.*, vol. 6, no. 5, pp. 1–11, 2014.
- [26] S. Cobos, M. S. Carvalho, and V. Alvarado, “Flow of oil-water emulsions through a constricted capillary,” *Int. J. Multiph. Flow*, vol. 35, no. 6, pp. 507–515, 2009.
- [27] Parr Instrument Company, *5100 5100 Low Pressure Reactors*. .

- [28] Parr Instrument Company, “Safety in the Operation of Laboratory Reactors and Pressure Vessels,” no. 230M, p. 8, 2005.
- [29] J. M. Velazquez, A. V. Gaikwad, T. K. Rout, J. Rzayev, and S. Banerjee, “A substrate-integrated and scalable templated approach based on rusted steel for the fabrication of polypyrrole nanotube arrays,” *ACS Appl. Mater. Interfaces*, vol. 3, no. 4, pp. 1238–1244, 2011.
- [30] B. J. M. Velazquez *et al.*, “Effective piezoelectric response of substrate-integrated ZnO nanowire array devices on galvanized steel,” *ACS Appl. Mater. Interfaces*, vol. 5, no. 21, pp. 10650–10657, 2013.
- [31] W. Stöber, A. Fink, and E. Bohn, “Controlled growth of monodisperse silica spheres in the micron size range,” *J. Colloid Interface Sci.*, vol. 26, no. 1, pp. 62–69, 1968.
- [32] ASTM International, “Standard Test Methods for Rating Adhesion by Tape Test 1,” pp. 1–9, 2017.
- [33] W. Zhang, N. Liu, Y. Cao, X. Lin, Y. Liu, and L. Feng, “Superwetting Porous Materials for Wastewater Treatment : from Immiscible Oil / Water Mixture to Emulsion Separation,” *Adv. Mater. Interfaces*, 2017.